2015

Factors affecting the heat transfer during the dip testing of potential third generation advanced high strength steels

Kramer Michael Pursell

Department:

FACTORS AFFECTING THE HEAT TRANSFER DURING THE DIP TESTING OF POTENTIAL THIRD GENERATION ADVANCED HIGH STRENGTH STEELS

by

KRAMER MICHAEL PURSELL

A THESIS

Presented to the Faculty of the Graduate School of the

MISSOURI UNIVERSITY OF SCIENCE AND TECHNOLOGY

In Partial Fulfillment of the Requirements for the Degree

MASTER OF SCIENCE IN METALLURGICAL ENGINEERING

2015

Approved by

Von L. Richards, Advisor
David C. Van Aken
Ronald J. O'Malley

ABSTRACT

A dip tester was designed and built at Missouri University of Science and Technology to test the effects of the primary alloying elements (Mn, Si, and Al) of Fe-Mn-Al-Si-C type 3rd generation advanced high strength steel (AHSS) alloys, dipping superheat, and dipping speed on the heat transfer during rapid solidification. The difficulties associated with casting 3rd generation AHSS were compiled as well to serve as a best-practices guide. An extensive list of potential 3rd generation AHSS alloys was developed and tested, and the effects of various dip testing parameters were examined.

Manganese was found to increase the heat flux by coating the copper blocks with MnO, reducing the air gap and improving the thermal conduction. Aluminum increased the heat flux by shifting the solidification path through multiple phase fields and thereby increasing the amount of enthalpy (heat) rejected upon solidification. The consequences however, were an increase in the secondary dendrite arm spacings and segregation within the microstructure resulting from a longer freezing range. Silicon was found to have no effect on the heat flux. It provided no substantial shift of the solidification path, nor did it increase the heat flux by improving the contact between the melt and copper blocks. Increasing the dipping superheat increased the heat flux by decreasing the melt viscosity and improving the wettability between the melt and copper blocks. An increase in the superheat also increased the driving force for heat transfer from the solidifying sample to the copper blocks.

ACKNOWLEDGEMENTS

My sincere gratitude is extended to Castrip, LLC for their funding as part of the project on 3rd Generation Advanced High Strength Steels Product Development.
I wish to thoroughly thank my adviser Dr. Von Richards for his motivation, support, and guidance during my time at Missouri S&T. I also wish to thank him for his insight into further development of my career upon my completion at Missouri S&T. I would also like to thank Dr. David Van Aken and Dr. Ron O'Malley for their support, guidance, and suggestions towards the success of this work. Dr. Simon Lekakh helped to further my understanding of true science and research, as well as in preparation for experimental heats and analysis. His help with CFD simulations and FactSage calculations is greatly appreciated as well. Dr. Kelvin Erickson's help with creating and reviewing the specifications and programming of the dip tester deserves my recognition. Dr. Rama Mahapatra, Peter Woodberry, Dan Edleman, Jay Watson, and Wal Blejde were helpful in providing support and experience during the development of the dip tester and design of experiments.

I would especially like to thank all of my colleagues and friends that I've gained during my time at Missouri S&T. In addition to the support and assistance with experiments and analysis, they have been more influential than they may ever know: Dan Field, Marc Harris, Jingjing Qing, Mingzhi Xu, Seth Rummel, Jun Ge, Obinna Adaba, and Scott Pisarik.

My wife, Sarah, and my family home in Indiana deserve most of my thanks for all of their support and continued interest in my research and studies. Their unending love and support during the difficulties and triumphs of all of my life's journeys has always made me believe in myself.

TABLE OF CONTENTS

Page

ABSTRACT iii

ACKNOWLEDGEMENTS iv

LIST OF ILLUSTRATIONS vii

LIST OF TABLES x

LIST OF ABBREVIATIONS (IN ORDER OF APPEARANCE) xi

SECTION

1. INTRODUCTION 1

1.1. BACKGROUND 1

1.1.1. High Mn Casting Best Practices 3

1.1.2. Direct Strip Casting in Industry 10

1.1.3. Laboratory-Scale Simulators 11

1.1.3.1 Dip testing 12

1.1.3.2 Melt spinning 17

1.1.3.3 Lab-scale horizontal single belt casting 19

1.1.3.4 Lab-scale twin roll caster 20

1.1.3.5 Laser surface remelting 22

1.1.3.6 Twin piston quenching and the hammer-anvil method 25

1.1.3.7 Melt splat and the gun quenching technique 28

1.1.3.8 Gas atomization 29

1.1.4. Conclusions 31

1.2. MOTIVATION FOR THIS WORK 32

2. EXPERIMENTAL PROCEDURE 33

2.1. DIP TESTING 33

2.2. POTENTIAL FOR FRACTIONAL SOLIDIFICATION 39

2.3. HEAT PROCEDURES 43

2.4. TESTING AND ANALYSIS PROCEDURES 49

3. RESULTS AND DISCUSSION 51

3.1. COMPARISON TO CURRENT CASTRIP ALLOYS AND OTHER WORK 51

3.1.1. Comparison to Current Castrip Grades 51

3.1.2. Comparison to Other Work 53

3.2. THERMOFLUID MODELING 57

3.3. EFFECT OF ALLOYING ELEMENTS ON HEAT TRANSFER 59

3.3.1. Effect of Manganese 59

3.3.2. Effect of Aluminum 62

3.3.3. Effect of Silicon 66

3.3.4. Effect of Carbon 67

3.3.5. Effect of Superheat and Dipping Speed 67

4. CONCLUSIONS AND RECOMMENDATIONS FOR FUTURE WORK 69

4.1. CONCLUSIONS 69

4.2. RECOMMENDATIONS FOR FUTURE WORK 69

APPENDIX 71

BIBLIOGRAPHY 72

VITA 79

LIST OF ILLUSTRATIONS

Page

Figure 1.1. Articles (source: Scopus) and patents (source: Free Patent) pertaining to twinning-induced plasticity steel research [1]. 1

Figure 1.2. Theoretical mechanical properties resulting from a prediction of the amount of martensite in dual phase steels [5]. 2

Figure 1.3. Alloy content variation across the ingot cast strip and the twin roll cast strip… 6

Figure 1.4. Cooling rates of the 8 lab-scale techniques examined in this work and 4 commercialized continuous casting processes. (TPQ- twin piston quenching) 11

Figure 1.5. A schematic of the dip tester apparatus used in the experiments by Strezov and Herbertson [59]. 12

Figure 1.6. The k-factor correlates fairly well with the heat flux [56]. 14

Figure 1.7. Metallurgical length during thin slab casting. 15

Figure 1.8. Increasing the superheat decreased the nucleation density in the first work done by Strezov and Herbertson [59] but increased in the later work done by Mukunthan et al. [56]. 16

Figure 1.9. A schematic of a melt spinning apparatus with both the melt and wheel contained in an inert atmosphere. 18

Figure 1.10. The two types of microstructures present in melt spun strips. 19

Figure 1.11. A drawing of the horizontal single belt casting simulator used by Guthrie et al. [72]. 20

Figure 1.12. A drawing of the lab-scale twin roll caster used by Lakshmikumar et al. [72]. 22

Figure 1.13. A drawing of the LSR process. [76]. 23

Figure 1.14. A phase map of the primary phases formed during solidification from examination of the microstructures of 7 Fe-Ni-Cr alloys solidified with various growth velocities [55] 24

Figure 1.15. A schematic of the hammer-anvil quenching apparatus with a photocell [25]. 26

Figure 1.16. Sequence of solute segregation during solidification 27

Figure 1.17. A drawing of the gun quenching apparatus used by Duwez and Willens [78]. 28

Figure 1.18. A schematic of the gas atomization process. 30

Figure 2.1. Dip tester setup. 34

Figure 2.2. The targeted time vs. distance of the bottom of the paddle from the melt surface dipping profile at a dipping speed of 60 m/min. 34

Figure 2.3. The distance from melt surface vs. velocity profile at a dipping speed of 60 m/min. 35

Figure 2.4. A plot of the temperature rise during a dip. 37

Figure 2.5. The target and actual velocity profiles as downloaded from the servo motor drive and PLC. 39

Figure 2.6. Fe-C phase diagram with the equilibrium solidification path of 0.2 wt% C shown. 40

Figure 2.7. Amount of liquid (LIQU), δ-ferrite (BCC_1), and austenite (FCC_1) present during equilibrium solidification, as calculated with FactSage. 41

Figure 2.8. Amount of liquid (LIQU), δ-ferrite (BCC_1), and austenite (FCC_1) present during Scheil solidification, as calculated with FactSage. 42

Figure 2.9. Dendritic growth across a sample from Alloy 5.2. 43

Figure 2.10. Samples generated from the dips at the 6 compositions of Alloy 7. 48

Figure 2.11. An immersion sample taken from the melt. 48

Figure 3.1. Heat flux and sample thickness for the alloys similar to the Castrip development grades 52

Figure 3.2. Schematic of the twin roll casting process. 52

Figure 3.3. Backscattered electron images (BEI) and compositional maps of a new Cr-coated copper block and the used Cr-coated copper block after 6 dips of testing Alloy 7. 54

Figure 3.4. Mn content vs. peak heat flux for Alloy 1 (0.3 wt% C and 0.3 wt% Si). 56

Figure 3.5. Size of the MnO particles on the block after the 6 dips during Alloy 7. 56

Figure 3.6. Air pockets caused by an air gap between the solidifying sample and the copper block. 57

Figure 3.7. The average heat flux and shell thickness of samples dip tested with various air gaps from ANSYS Fluent simulations 58

Figure 3.8. Mn content vs. k-factor for Alloy 7 (0.18 wt% C, 2.7 wt% Si, and 0.1 wt% Al) 59

Figure 3.9. Air pockets in the Alloy 5.2 samples after consecutive dips 60

Figure 3.10. FactSage calculations of the stable oxide formation in an alloy of 0.3 wt% C, 2.5 wt% Si, 7 wt% Mn, and 50 ppm O. 62

Figure 3.11. Aluminum content vs. average heat flux for Alloy C (0.25 wt% C, 0.6 wt% Mn, and 2.5 wt% Si). 63

Figure 3.12. Phase diagram for Alloy C with varying aluminum contents, as calculated with FactSage 64

Figure 3.13. The amount of heat released during solidification from the initial dipping temperature to the solidus temperature for varying aluminum contents of Alloy C, as calculated with FactSage 64

Figure 3.14. Aluminum content vs. average secondary dendrite arm spacing (SDAS) ... 65

Figure 3.15. Silicon content vs. average heat flux for Alloys 2A (0.2 wt%C and 3.5 wt% Mn) and 2C (0.2 wt% and 8 wt%). 66

Figure 3.16. Average heat flux as a function of casting speed and superheat for Alloy AC (0.2 wt% C, 7.5 wt% Mn, 2.5 wt% Si, and 2 wt% Cu). 67

LIST OF TABLES

Page

Table 1-1. Alloy compositions and processes studied for the references in the casting and processing of Fe-Mn-Al-Si-C alloys literary survey. 8

Table 1-2. References to the studies, the sample sizes produced, and the method of temperature measurement for the rapid solidification processes examined in this work..... 31

Table 2-1. Coefficients for Equation 2-2 as a function of the distance of the thermocouples from the surface of the copper blocks. 38

Table 2-2. Compositions, dipping superheats, and dipping speeds of the alloys tested... 44

LIST OF ABBREVIATIONS (IN ORDER OF APPEARANCE)

Abbreviation	Description
AHSS	advanced high strength steel
TRIP	transformation-induced plasticity
DSC	direct strip casting
TWIP	twinning-induced plasticity
SFE	stacking fault energy
TSC	thin slab casting
ISFE	intrinsic stacking fault energy
USFE	unstable stacking fault energy
M_s	martensite start
SDAS	secondary dendrite arm spacings
PDAS	primary dendrite arm spacings
LSR	laser surface remelting
TPQ	twin piston quenching
PLC	programmable logic controller
DAQ	data acquisition
SEM	scanning electron microscope
XRD	x-ray diffraction
EDS	energy dispersive spectroscopy

1. INTRODUCTION

1.1. BACKGROUND

A significant amount of work has been done to develop a steel which exceeds the properties of 1st generation advanced high strength steels (AHSS) but at a lower cost than that for 2nd generation AHSS; the steels which fit into this category are termed 3rd generation AHSS. Currently the body in white portion of vehicles accounts for approximately 20% of the vehicle's mass [1], and the stiffness of the components is more dependent on design geometry than material properties [2]. Although it is apparent that improvements in fuel economy and safety cannot come from an advancement in materials alone, a significant push is being made for a reduction in the vehicle weight while maintaining a sound passenger compartment. The driving force for this work, which has seen an increase in focus in recent years as evidenced in Figure 1.1 [1], are the penalties associated with not meeting the CAFE standards of 54.5 miles per gallon coming in 2025.

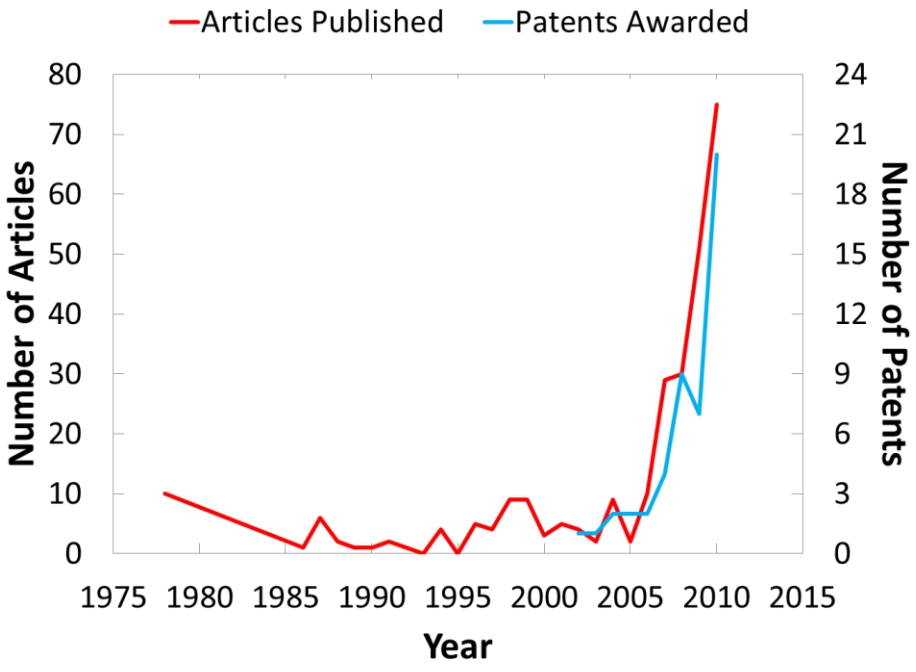

Figure 1.1. Articles (source: Scopus) and patents (source: Free Patent) pertaining to twinning-induced plasticity steel research [1].

The current methods of reaching the 3rd generation space have been through changing the alloying contents of current 1st and 2nd generation AHSS by or by advanced heat treatments. Specifically, the Mn, Al, Si, and C contents in Fe-Mn-Al-Si-C-type steels have been varied [3,4]. Quench and partition, dual phase, complex phase, and austempering heat treatments have been investigated [5] also. Both of these routes yield microstructures with a combination of austenite, martensite, bainite, or ferrite. The proportions of these phases play a strong role in the final mechanical properties as shown in the dual phase systems in Figure 1.2 [5]. It is the interactions within the microstructures, such as dynamic strain aging, dynamic Hall-Petch effects [6], and the interaction of Mn-C clusters around dislocations [7], which produce the exceptional strength and ductility.

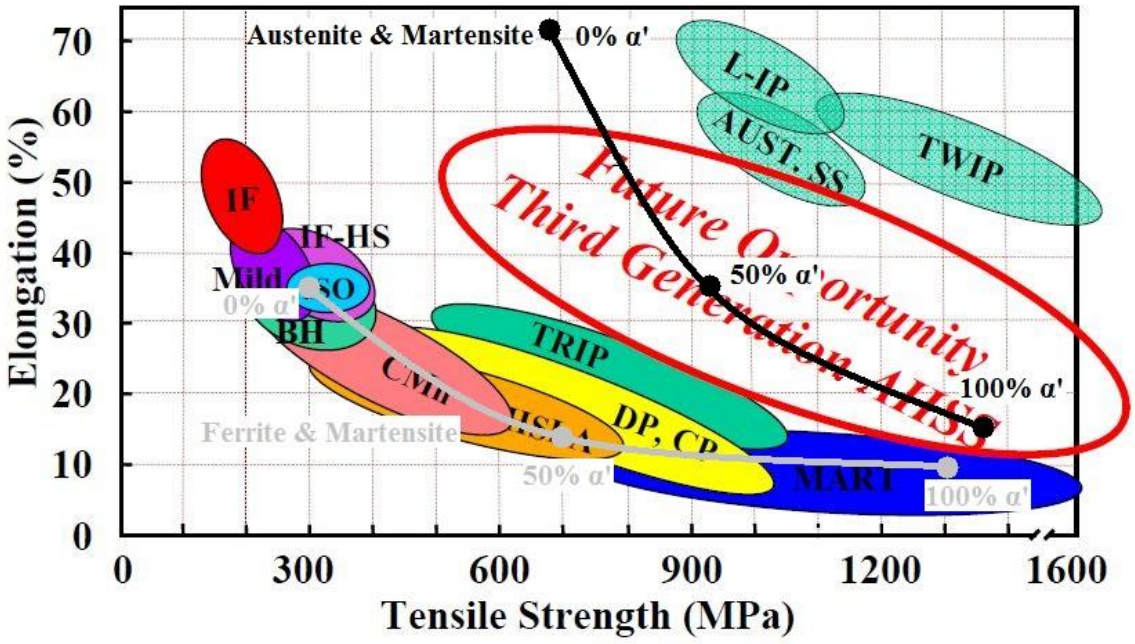

Figure 1.2. Theoretical mechanical properties resulting from a prediction of the amount of martensite in dual phase steels [5].

In addition to original research on casting and solidification characteristics of various 3rd generation AHSS alloys contained later in this work, a summary of a literature

search is provided in the next section to give suggested practices for commercially casting 3rd generation transformation-induced plasticity (TRIP) alloys. In particular, the casting and processing difficulties, inclusion control, experimental evidence for the best casting and processing practices, a comparison of direct strip casting (DSC) and conventional casting, and the effects of alloying elements are detailed.

Following the best-practices section, a review and summary of several lab-scale methods of testing alloys under rapid solidification conditions is presented. From the review, the most efficient method of testing is identified.

1.1.1. High Mn Casting Best Practices. Fe-Mn-Al-Si-C alloy casting difficulties. Some of the difficulties associated with casting highly alloyed steels are fairly obvious. The aggressive slags and propensity for dirty steels which are caused by the inclusions are products of using alloying elements with stable oxides such as aluminum, silicon, and manganese. These slags have the tendency to react with, dissolve, and erode the refractories. The desire for multi-phase steels with high contents of elements that tend to segregate leads to banding which is difficult or impossible to remove during subsequent processing [8]. The tramp elements which are introduced to the melt with ferro-alloy additions, and even commercially pure alloys, can exacerbate the issues of inclusions and segregation. High purity alloys must be used as much as possible, but these additions drive up costs. High manganese alloys form a very strong outer shell during solidification [8]. In fact, they are four times stronger than some ferritic grades [9]. These alloys exhibit a brittle temperature range of approximately 900-1300°C which can lead to hot tearing [10].

Second generation AHSS contain high levels of aluminum. Wang et al. saw AlN and Al_2O_3 inclusions at the tips of severe edge cracks in the Fe-23Mn-3Al-3Si-0.03C (all wt%) twinning-induced plasticity (TWIP) steel strip produced by ingot casting and hot rolling. In contrast, edge cracks were not seen in the strip produced by twin roll casting [11]. It is deduced that inclusions at the crack tips were a result of agglomeration during casting. Twin roll casting is known to produce a fine dispersion of inclusions instead of large agglomerations [12].

Calcium and rare earth elements have been shown to be effective at modifying and reducing the amount of inclusions in steel. A Ca/Al ratio greater than 0.14 and Ca/S

ratio greater than 0.7 decreases the amount and size of inclusions in the construction steels studied. The inclusions that remained were more plastic than those remaining with less Ca-treatment [13]. Calcium treatment should be used with caution in automotive steels because the resulting modified inclusions reduce the deep-drawability [14]. Grajcar et al. showed that a mischmetal addition could be used to reduce the amount of inclusions, as well [15]. The ideal amount of rare earth elements to be added should be between 0.77 g per kg of steel [16] and 1.74 g per kg of steel [15]. However, melt treatment with rare earth elements is not without its difficulties. Inclusions formed with rare earth elements are denser and therefore more difficult to float out [17]. Rare earth elements can also form low melting point eutectics with alloying elements and decrease the high temperature ductility [15].

Pisarik et al. showed that the processing history can affect the formation of epsilon martensite in 3rd generation TRIP steels and make it easier or more difficult to achieve TRIP or TWIP behavior [18]. As such, the casting and post-processing parameters must be given due consideration as well. The research group operating the lab-scale twin roll caster at Aachen University has made strides to determine optimum casting practices for casting 20-30 wt% Mn steels. From their experiments, a high roll closing force should be used to minimize porosity as the strip comes together at the roll nip [19]. The use of sintered BN-SiO_2 side dams is preferred over SiO_2 side dams which were rapidly eroded by the aggressive slag [20].

After casting, an in-line hot reduction of at least 15% was shown to close 10-30 μm of remaining porosity and significantly improve the strip surface quality [19,20]. Deformation may also produce unintended microstructural modification during cooling. Grajcar et al. suspected that straining the prior austenite shifts the ferrite start to shorter times in the associated continuous cooling transformation diagrams and saw small amounts of unexpected primary ferrite after repeated hot deformation of ingot-cast material [21]. Rolling reductions can be used to decrease the austenite grain size and increase the mobility of austenite stabilizers [22].

One of the major advantages of twin roll casting is the inherent reduced dendrite arm spacing, which reduces the scale of chemical inhomogeneities, i.e. segregation.

Homogenization at 1150°C for 2 hours was required to completely dissolve the dendritic microstructure present from twin roll casting [20].

Aydin et al. showed the annealing temperature where the maximum amount of austenite occurs at increases with increasing manganese content. Additional carbon diffusion to the austenite during the annealing process improves the stability of the austenite at room temperature [23]. In the austenite and bainite dual phase steel produced by Martis et al., there was a tradeoff between achieving a high amount of retained austenite and fine bainite plates. They found the highest strength and toughness occurred when the dual phase steel was austempered at low temperatures. At these low temperatures the bainite was finer and the austenite was saturated with carbon, and therefore more stable at room temperature [24].

There have been a few studies to highlight the benefits of twin roll casting in comparison to thin slab casting (TSC) and ingot casting. Ingot casting is the only current method of commercially producing these Fe-Mn-Al-Si-C alloys because of their poor castability via thin slab casting; and has therefore been the basis of comparison in many studies [10,19]. The benefits associated with twin roll casting make it a viable tool to combat the difficulties with casting Fe-Mn-Al-Si-C alloys. The benefits of rapid solidification have been detailed elsewhere [25-29] and include: a reduction in solute segregation, extended solid solubility, refinement of microstructures, and the formation of metastable phases. The twin roll casting process can add to this list: freedom from reactive mold powders, better strip surface quality, and smaller and more dispersed inclusions.

As previously mentioned, the primary alloying elements- C, Mn, Si, and Al- have a tendency to segregate. Rapid solidification can be employed to minimize the amount of segregation as shown by Daamen et al. in Figure 1.3 [20]. In addition, the bulk chemistry is more consistent due to the lack of decarburization and oxidation from frequent reheating, as is required when processing from an ingot. The tramp elements have been shown to distribute evenly as well [30,31]. δ-ferrite formation was suppressed by the high cooling rates in the work done by Liu et al. [32]. This could prove very important as the industry pushes to reduce the manganese content to make the alloy more castable. Reduced manganese levels increase the likelihood for δ-ferrite to form on solidification.

The grain refinement associated with rapid solidification increases the critical resolved shear stress which delays twinning [33,34]. Alloys cast by twin roll casting have been shown to have ultimate tensile strengths and elongations similar to those cast by conventional methods [10,11].

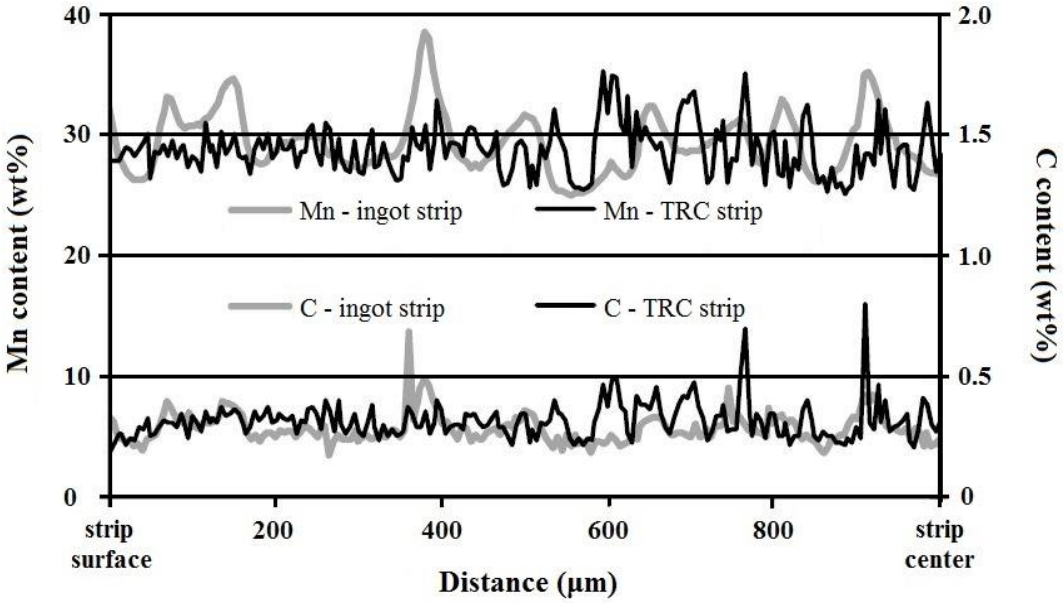

Figure 1.3. Alloy content variation across the ingot cast strip and the twin roll cast strip. The target contents were 29 wt% Mn and 0.3 wt% C [20].

The elimination of mold powders in the twin roll process allows for increased concentrations of reactive alloying elements such as manganese and aluminum in the steel. The surface quality of the strip is better than that produced by ingot casting because the strip contains reduced scale, since the strip requires less hot rolling to reduce the strip to the required gauge thickness. In ingot-cast slabs, the scale must be removed and can be rolled into the strip during hot rolling, causing surface defects. Also previously mentioned was the formation of small well-dispersed inclusions [12]. There is a tendency, however, for endogenous inclusions to end up in the center of the strip, whereas exogenous inclusions are evenly distributed [20]. The likelihood of exogenous inclusions in twin roll cast strip is reduced because mold powders are not used.

There has been good agreement on the effect of alloying elements in the development of TRIP and TWIP alloys and in their castability. Manganese (7-30 wt% typical) is a known austenite stabilizer, and therefore a primary constituent in these multi-phase alloys. It is also known to lower both the unstable stacking fault energy (USFE) and the intrinsic stacking fault energy (ISFE) [4]. The USFE can be thought of as the barrier to nucleate dislocations for plasticity and form ε-martensite, where large positive values make it harder to form; while the ISFE is often realted to the mechanisms of TWIP and TRIP. It should be noted that low ISFE favors the stability of the ε-martensite. The ability to transform from austenite to ε-martensite without over-stabilization of the ε-martensite is crucial to the effectiveness of dual TRIP alloys and produce the 3rd generation properties [18].

Aluminum (0.5-2 wt% typical) decreases the USFE but increases the ISFE, making ε-martensite easier to form but also easier to transform to α-martensite [4]. It can increase the intrinsic stacking fault energy enough to suppress the TRIP mechanism and cause only TWIP [35]. The addition of aluminum has been shown elsewhere to reduce the amount of retained austenite [5]. Aluminum has a unique effect on the diffusivity of carbon in austenite. It has been seen to aid partitioning of carbon to the austenite [2], and decrease the activity and diffusivity of carbon from the austenite [36], resulting in delayed cementite formation [2, 36]. In another comparison of ingot casting and twin roll casting, aluminum segregates to the interdendritic regions in cast ingots but not in twin roll cast strip [11].

The obvious danger of using aluminum is δ-ferrite formation. δ-ferrite is a non-transformable phase which produces stringers during rolling, yielding to anisotropy in rolled steel. δ-ferrite is seen as detrimental when the desire is to maximize the amount of transformable phases. Silicon (1-3 wt% typical) can be used to produce similar effects as aluminum on the USFE and ISFE with less of a risk for δ-ferrite formation [4]. It is theorized the manganese content must be greater than 12 wt% and the aluminum content must be kept below 2.9% when higher silicon contents are used [37]. Silicon decreases the generalized stacking fault energy and promotes the TRIP transformation of $\gamma \rightarrow \varepsilon$ [38]. Silicon has also been shown to prevent carbide formation during austempering [39] and is therefore present in many “carbide-free bainite” steels. Silicon causes issues during

galvanizing because it forms a stable oxide on the surface [40]. This can be counteracted by annealing in a hydrogen atmosphere to reduce the oxide scale [41].

Carbon (0.06-0.15 wt% typical) is the most mobile austenite stabilizer, and many heat treatments targeting 3rd generation properties seek to exploit this. Excess partitioning of carbon in some steels can over-stabilize the ε-martensite and cause premature failure and eliminate the dual TRIP characteristics [37]. Carbon additions decrease both martensite start (M_s) temperatures.

Minor amounts of nitrogen, and niobium have been shown to have effects on the microstructure as well. Nitrogen is an austenite stabilizer and has been used in increased amounts for just that [5]. Less than 0.04 wt% Nb has been used as an austenite stabilizer and to attempt to grain refine the microstructure. It was found that increased amounts of manganese and aluminum in these alloys prohibit the typical formation of the grain-refining Nb(C,N) precipitates [21]. Niobium in solution increases the generalized SFE, reducing the ε-M_s temperature. 0.017 wt% Nb raised the SFE in the material enough to produce a material, which underwent TRIP without the niobium addition, to only TWIP at temperatures down to -75°C [42].

Table 1-1 lists the compositions and processes studied within the sources contained in the review of the best practices for casting high Mn alloys.

Table 1-1. Alloy compositions and processes studied for the references in the casting and processing of Fe-Mn-Al-Si-C alloys literary survey.

Reference and Authors	Composition (wt%)	Process Examined
[2] Kuziak et al.	0.06-0.15% C, 1.5-2.5% Mn, Si, <0.4% Cr & Mo, <0.6% V, <0.04% Nb	Heat treatments and properties
[4] Pisarik et al.	0.08% C, 15.1% Mn, 2% Si, 1.4% Al and 0.16% C, 14.3% Mn, 3% Si, 0.9% Al	Sand casting, heat treatments, and properties
[8] Gigacher et al.	0.5% C, 25% Mn, 1% Al	High temperature strength
[10] Daamen et al.	0.6% C and 22% Mn	Twin roll casting, heat treatments, and comparison of DSC vs. conventional casting

Table 1-1. Alloy compositions and processes studied for the references in the casting and processing of Fe-Mn-Al-Si-C alloys literary survey (cont.).

Reference and Authors	Composition (wt%)	Process Examined
[11] Wang et al.	23% Mn, 3% Si, 3% Al	Twin roll casting, properties, and comparison of DSC vs. conventional casting
[15] Grajcar et al.	0.04-0.07% C, 24-28% Mn, 3-4% Si, 1.6-3% Al, 0.3% Nb, mischmetal additions	Vacuum induction melting and modification of inclusions by mischmetal additions in FeMnAlSiC alloys
[18] Pisarik and Van Aken	0.02-0.24%C, 14-22% Mn, 0.2-3% Si, 0.9-3% Al	Thermodynamics of the $\gamma \rightarrow \varepsilon \rightarrow \alpha'$ transformation
[19] Daamen et al.	0.3% C, 29% Mn, 0.001% Al	Twin roll casting, heat treatments, and mechanical properties
[20] Daamen et al.	0.3% C, 29% Mn	Twin roll casting and heat treatments
[21] Grajcar et al.	0.17% C, 3% Mn, 0.2% Si, 1.7% Al	Ingot casting, thermomechanical processing, and effects of microalloying (0.04% Nb)
[23] Aydin et al.	0.1-0.2% C, 5-10% Mn, 3% Si, 3% Al	Ingot casting, heat treatments, and properties
[24] Martis et al.	0.3% C, 0.4% Mn, 2% Si	Austempering of a low-C, low alloy steel
[32] Liu et al.	0.1% C, 26% Mn, 22% Cr, 2% Si, 0.04% Al	Twin roll casting and mechanical properties
[35] Ishida and Nishizawa	0.5-1.3% C, 17% Mn, 1-3% Si, 0.6-2.5% Al, and several others (Cu, Cr, Mo, Ni, etc)	Dilatometry to determine the effect of alloying elements on ε-martensite stability
[37] Van Aken et al.	0.06% C, 14% Mn, 1.85% Si, 2.4% Al	Sand casting and mechanical properties
[38] Schramm and Reed	0.01-0.9% C, 1-16% Mn, 0.3-1.3% Si, 5-30% Cr, 4-34% Ni	SFE calculations and XRD determination of phases present in various alloys
[42] Huang et al.	0.01% C, 22% Mn, 2% Si, 1.85% Al	Ingot cast, low temperature tensile tests, and effects of microalloying (0.014% Nb)

1.1.2. Direct Strip Casting in Industry. Many large-scale steelmakers have sought to exploit the benefits of direct strip casting (DSC) on an industrial scale. In 2012 Ge et al. listed the Castrip and poStrip operations as the twin roll casting processes currently in full-scale operation [43] with a few others still in development. The maximum production at the Castrip plants in Crawfordsville, IN and Blytheville, AR are 500,000 tons per year each [44] while the poStrip plant in Pohang, South Korea is higher at 600,000 tons annually [43]. Baosteel in China is one of those in development, with the building of a pilot plant in China for the development of their Baostrip process [45]. SMS Demag, MAIN AG, Corus Research, and Lucerne University have worked together since the early 2000s to produce plans and a pilot plant for casting stainless and low-carbon steels through the MAINSTRIP twin roll casting process [46,47]. Several unique design features allow for the expected annual production to be between 300,000-800,000 tons [48-51]. Salzgitter Flachstahl GmbH in Germany has built the only currently commercialized horizontal single belt caster after development work on a pilot plant at TU Clausthal. It is expected this horizontal single belt caster, commissioned in 2013, will prove a contender in the strip casting industry with production of advanced high strength steels to peak at 25,000 tons per year [43,52]. The twin roll casting and horizontal single belt casting processes are the only two currently commercialized means of producing ultra-thin cast strip in the steel industry.

The commercialized processes have experienced difficulties in rapidly solidifying steel. Water cooling is a necessity to transfer the large amounts of heat associated with rapid solidification. The requirement for controlled casting atmospheres was borne out of the detriment of inclusions to the ultra-thin strip quality [53]. Surface defects a few microns deep represent a larger portion of the 1-6 mm cast strip than in thin slab casters where the slabs are 50-60 mm thick.

Alloys cast on a day-to-day basis at Castrip in Crawfordsville, IN are low-C grades with carbon contents near 0.035 wt%, manganese contents less than 1 wt%, and silicon contents between 0.2-0.3 wt% [54].

1.1.3. Laboratory-Scale Simulators. Representing these industrial processes in a laboratory requires careful control and monitoring of several variables such as heat flux, sample thickness or diameter, cooling rate, and melt delivery method. Some of these variables are interdependent as explained in this work via the governing equations for the particular process. The techniques listed in this work are used to control and monitor these variables in different ways and are capable of producing rapidly solidified samples in a variety of shapes at different cooling rates as shown in Figure 1.4.

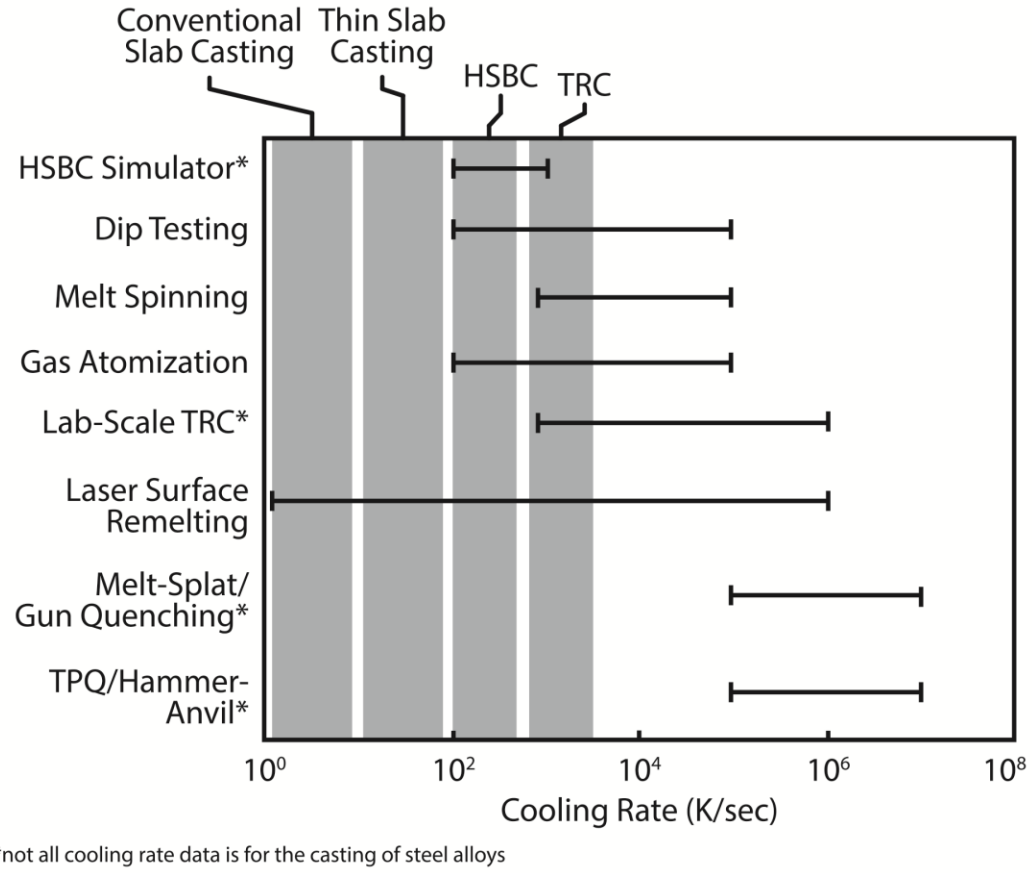

Figure 1.4. Cooling rates of the 8 lab-scale techniques examined in this work and 4 commercialized continuous casting processes (TPQ- twin piston quenching).

Elmer et al. list the generally accepted cooling rate requirement for rapid solidification to be in the range from 10^3 to 10^7 K/sec [55]. It has been shown these cooling rates are required to achieve the benefits listed previously in Section 1.1.1

[26,27,56-58]. The laboratory techniques discussed here which have been developed to achieve such cooling rates are: dip testing, melt-spinning, lab-scale horizontal single belt casting and twin roll casting processes, laser surface remelting, twin piston quenching and hammer-anvil, gun quenching and melt splat, and gas atomization.

1.1.3.1 Dip testing. The method of rapidly submerging and retracting a substrate from a steel melt with an automated servo motor is a relatively new process and has become known as dip testing. Blocks of pure copper or a copper alloy are typically used as the substrate due to their high thermal conductivity and approximation to the copper rolls used in commercialized twin roll casting processes. A schematic of the system used by Strezov and Herbertson is shown in Figure 1.5 [59].

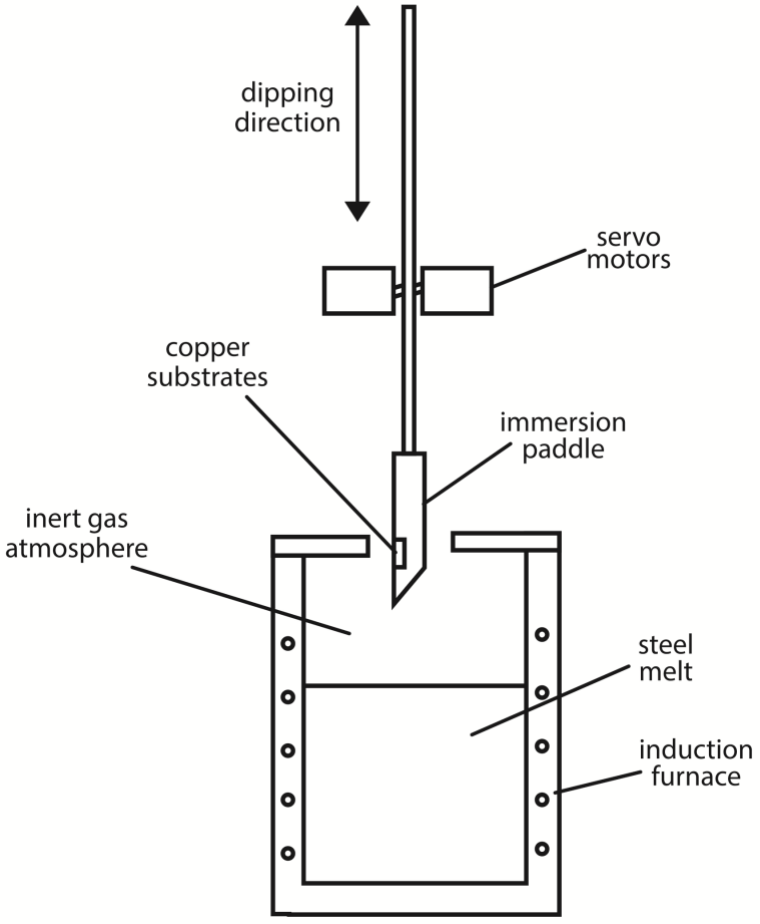

Figure 1.5. A schematic of the dip tester apparatus used in the experiments by Strezov and Herbertson [59].

The sample is solidified by heat extraction through the copper substrate. It is known that the gas layer between the substrate and solidifying sample plays an important role in heat transfer [56,59]. Extensive work has been done to determine the effect of the surface texture of the copper blocks and the influence of an inert gas atmosphere over the melt in removing heat and promoting surface nucleation on the copper substrate [59]. Thermocouples embedded at a precise distance from the surface of the substrate are used to measure the temperature increase as the blocks are rapidly "dipped" into a steel melt that is typically contained within a lab-size induction furnace. The data recorded by the thermocouples is then used to calculate the heat flux by Beck's inverse heat conduction method or by relations to known boundary conditions [59,60]. The typical cooling rate in the dip testing process is on the order of 10^3 K/sec but can be as high as 10^6 K/sec [61].

Strezov and Herbertson varied the substrate texture, melt superheat, gas atmosphere, and dipping velocity to make many observations for 304 stainless steel [59]. These studies show that a textured substrate produced a higher heat flux and a higher nucleation density than smooth substrates. The explanation was that the textured substrates provide more heterogeneous nucleation sites. They noticed a slight increase in the heat flux when the melt cover gas was changed from argon to helium. This minor change in heat flux did not correspond to a difference in the microstructure or the nucleation density. Increasing the velocity of the dip also increased the maximum heat flux, nucleation density, and produced a finer microstructure. Dipping at a higher superheat led to an undesirable decrease in the maximum heat flux, nucleation density, and microstructural refinement.

The effect of increasing the superheat and changing the gas atmosphere from nitrogen to argon during dip testing Fe-Cr-Al alloys was done in a more recent experiment by Mukunthan et al. [56]. They used a k-factor as described in Equation 1-1 to compare the results between dips, in addition to the data measured by the thermocouples in the copper blocks. The k-factor is useful when comparing the differences in thickness between samples and also takes into account the duration of the dip, two factors directly related to the heat flux. The equation is provided as Equation 1-1 [56]. The heat flux is higher for thicker samples when the time in the melt is the same.

$$k = \frac{d}{\sqrt{t}} \qquad \text{Eq. 1-1}$$

k is the k-factor which gives an approximation of the solidification rate, *d* is the thickness of the solidified sample, and *t* is the time in the melt. The k-factor showed a reasonable trend with relation to the heat flux measured by thermocouples in the copper blocks, but did have a bit of variability as shown in Figure 1.6 [56].

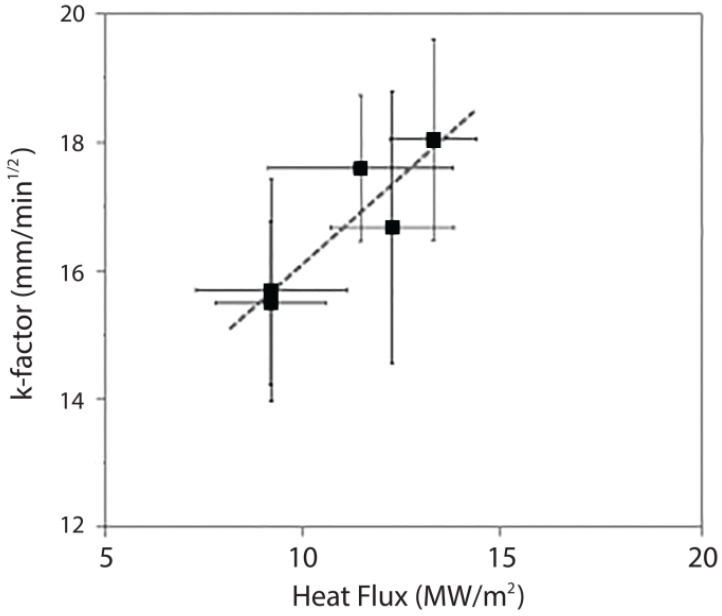

Figure 1.6. The k-factor correlates fairly well with the heat flux [56].

In continuous casting of steel, the distance from the mold to the location where the cast slab has completely solidified is called the metallurgical length. The metallurgical length is shown schematically in Figure 1.7. The k-factor can be used in continuous casting operations as an approximation of the metallurgical length through Equation 1-2. The metallurgical length is useful in determining if the alloy is castable or not. If the metallurgical length is longer than the maximum length at which a caster can safely operate, the alloy cannot be cast. Too short of a metallurgical length can be harmful as well because many of the austenitic TRIP alloys have high strengths at

elevated temperatures [8-10], as was mentioned in Section 1.1.1.1. Therefore, the casting speed must be carefully selected so the melt solidifies at the proper time. Casting speed can often be reduced to bring the metallurgical length within acceptable casting requirements, but at the penalty of increased operating costs.

$$L = V \left(\frac{d}{k}\right)^2 \qquad \text{Eq. 1-2}$$

Where L is the metallurgical length, V is the casting speed, d is the thickness of the solidified strip, and k is the k-factor.

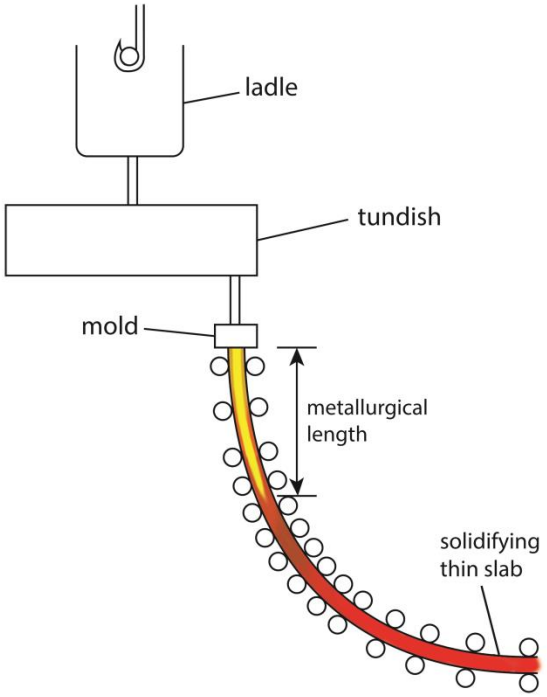

Figure 1.7. Metallurgical length during thin slab casting.

Mukunthan et al. also noticed an increase in the heat flux when the cover gas was changed from argon to nitrogen gas with a higher conductivity. No observed change in the microstructure was associated with the change in dipping atmospheres. Mukunthan et

al. reported that an increase in the superheat led to an increase in the nucleation density and heat flux in the 15Cr-4Al alloy they studied, which is contrary to the previous work done with 304 stainless steel by Strezov with Herbertson [56].

Mukunthan et al. proposed the increase in driving force for nucleation at low superheats increased the heat flux in the first work by Strezov and Herbertson [56,59]. In the later work by Mukunthan et al., the superheats were large enough to decrease the melt viscosity and increase the wettability; and thus at overcame the reduction in driving force for nucleation [29,56,62]. The measurable effects of increased driving force at low superheats and increased wettability at high superheats are an increase in the nucleation density and heat flux, respectively. The data from the two studies are presented in Figure 1.8 [56].

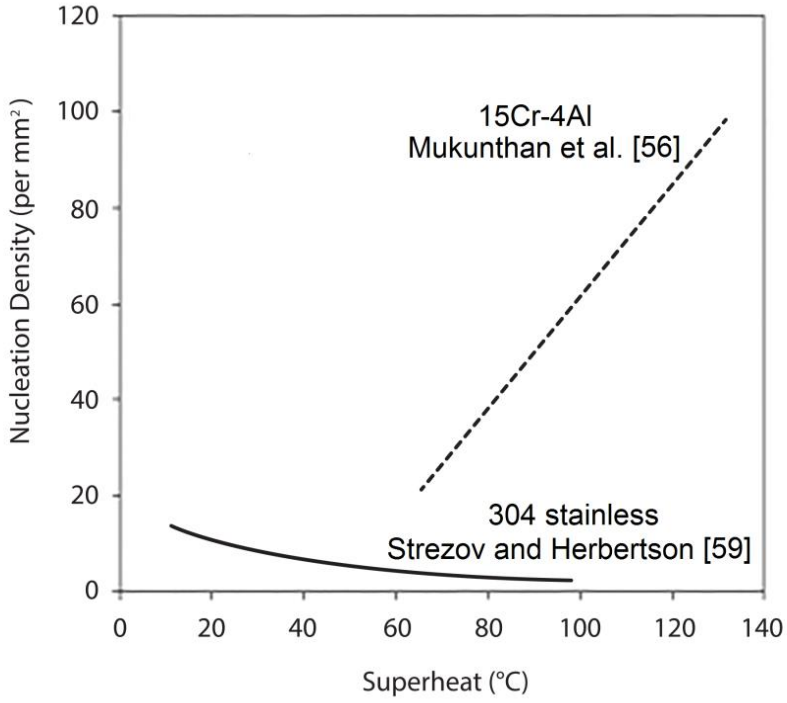

Figure 1.8. Increasing the superheat decreased the nucleation density in the first work done by Strezov and Herbertson [59] but increased in the later work done by Mukunthan et al. [56].

It is the ability to modify the heat flux and match actual casting parameters- such as casting speed, gas atmosphere, substrate texture, and dipping superheats, which make dip testing ideal for simulating industrial rapid solidification processes. In addition, the process can be closely monitored with embedded thermocouples and continuous feedback can be used to control the servo motor.

Figure 1.4 shows that the range over which the heat flux can be varied in dip testing is very near those encountered with industrial twin roll casters and horizontal single belt casters. This process has been used to determine the feasibility and expected success of casting various alloys under different conditions in the Castrip process at a BlueScope Steel research facility [63]. Researchers at BlueScope, one of the three member companies of Castrip, have done extensive experiments to model the solidification and nucleation during the dipping process [61].

In some studies, mechanical tests can be performed directly on the solidified sample. Lucas et al. have shown the thin samples produced by dip testing can be mechanically tested with an instrumented shear punch to obtain a stress-strain curve [64].

1.1.3.2 Melt spinning. The process to produce a thin ribbon at cooling rates of 10^5 K/sec [65] on a rotating copper wheel is melt spinning. A high pressure inert gas is used to push the melt out through a small hole in a crucible above the spinning wheel as shown in Figure 1.9. The process was first patented in the U.S. in 1958 to produce thin metal filaments [66].

The temperature of the melt and rotating wheel can be measured to approximate the heat flux. Chen et al. measured the secondary dendrite arm spacings (SDAS) and calculated the cooling rate using equations published for the particular Fe-Cr-Mn-C alloy they studied [65]. The SDAS varies with cooling rate unlike the primary dendrite arm spacings (PDAS). The general equation relating the SDAS to the cooling rate is given in Equation 1-3 [64].

$$\lambda_2 = a \cdot \dot{T}^{-n} \qquad \text{Eq. 1-3}$$

Where λ_2 is the SDAS, $\dot{T}$ is the cooling rate, and a and n are experimentally determined fitting parameters. Work is continually being done with different alloys and

solidification practices to develop more accurate and comprehensive models to relate the SDAS to the cooling rate [67-69].

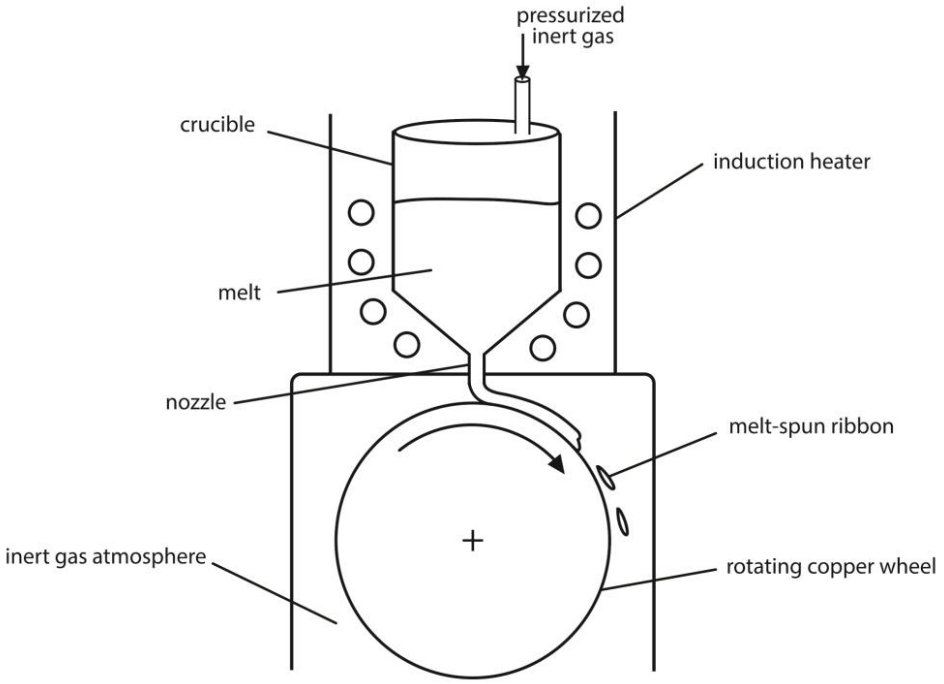

Figure 1.9. A schematic of a melt spinning apparatus with both the melt and wheel contained in an inert atmosphere.

The rotational velocity of the wheel can be varied to produce changes in the heat flux, making this process favored for simulating a variety of cooling rates. Chen et al. saw the best surface quality in their Fe-Cr-Mn-C steel ribbons at a rotational velocity of 13-16 m/sec and a cooling rate of 7-22x10^5 K/sec. When the surface of the ribbon was in poor contact with the roll, air pockets developed and an equiaxed grain structure formed adjacent to the air pockets. The microstructure shifted to dendritic in the region away from the initial solidification surface [65] as in Figure 1.10a. The austenitic Fe-Ni studied by Hayzelden et al. showed a segregation-free zone near the surface in contact with the roll and transitioned to a dendritic microstructure farther from the surface [70] as in Figure 1.10b. An increase in the microstructure size and/or change in morphology away

from the contact surface were also noted in dip testing [58] and twin piston quenching [70].

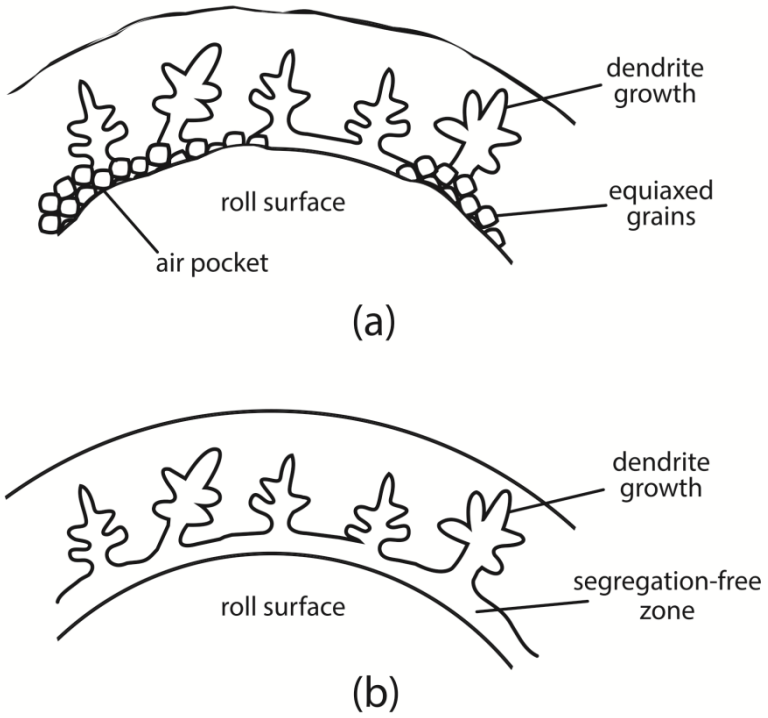

Figure 1.10. The two types of microstructures present in melt spun strips. Microstructure in the strip with (a) poor contact with the casting roll and (b) good contact with the casting roll.

1.1.3.3 Lab-scale horizontal single belt casting. Lab-scale setups of industrial rapid solidification processes can yield more useful samples and results than the previously mentioned methods. A lab-scale horizontal single belt caster like that at the McGill Metal Processing Center at McGill University can be used to accurately determine the effect of various casting parameters such as substrate texture, casting superheat, and alloy grade [71,72].

An apparatus designed to simulate the horizontal single belt casting process was also built at the McGill Metal Processing Center. This apparatus allows for five textured copper blocks to be placed in a fixture which is propelled by a spring while molten metal

flows in from above the substrates. The apparatus is capable of producing heat fluxes as high as 12 MW/m^2 and cooling rates of 10^2 K/sec, for the casting of aluminum [72]. High precision thermocouples embedded in the copper blocks allow for monitoring of the temperature rise during the initial stages of solidification. The apparatus is shown schematically in Figure 1.11.

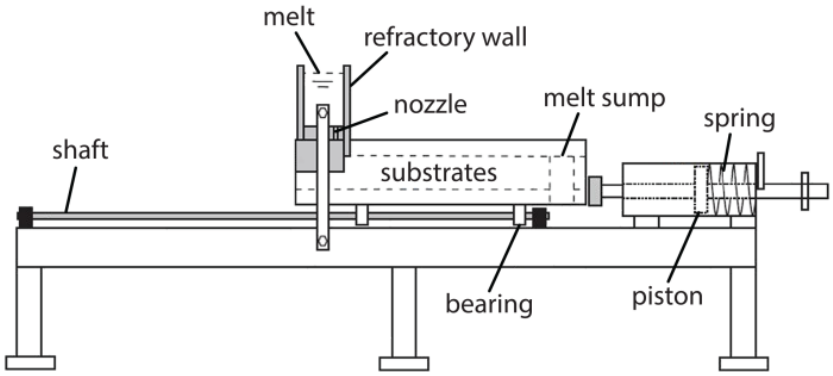

Figure 1.11. A drawing of the horizontal single belt casting simulator used by Guthrie et al. [72].

The simulator apparatus has been used to investigate the initial moments of solidification in the horizontal single belt casting and twin roll casting industrial processes. One avenue of analysis has been the consequent experiments and modeling of the formation of a small gas layer and heat flux through the entrapped layer. From there, the heat flux, nucleation density, and strip quality have been related back to the presence of the gas layer [72]. Changing the gas atmosphere at the meniscus area has resulted in suggestions for improving the strip quality of aluminum sheet produced by horizontal single belt casting. It was found an oxygen atmosphere nearly eliminated all of the air pockets, improving the strip surface and eliminating the need for the graphite coating applied to the casting substrates [71].

1.1.3.4 Lab-scale twin roll caster. Another industrial process scaled down for laboratory use is the twin roll casting process. Work was done in 1980 by Lakshmikumar et al. using alloys known to produce amorphous phases under rapid

solidification conditions [73]. The cooling rate was not directly measured during the test; instead it was estimated both by calculations from the SDAS and by observations of amorphous phases. The approximated cooling rates were on the order of 10^6 K/sec in the indium-tellurium and copper-gold-tellurium alloy systems they studied. The appearance of amorphous phases seen in the samples indicate the cooling rates were of at least the same magnitude as that achievable in the later-discussed gun quenching technique [73]. The system used by Lakshmikumar et al. is shown schematically in Figure 1.12.

The lab-scale twin roll caster at Aachen University has been utilized in the recent development of the Eurostrip twin roll casting program [74]. Aachen University's casting system is designed for the production of AHSS with 30 wt% Mn and 3 wt% Al [19]. Strips 2 mm thick by 150 mm wide of 0.3 wt% C and 29 wt% Mn were successfully cast, hot rolled, subsequently cold rolled and finally annealed; all continuously within the lab. This work proves that alloys that are difficult to cast by traditional methods can be produced by twin roll casting. Daamen, et al. of Aachen University have also shown the benefits of twin roll casting compared to the more energy-intensive thick slab casting in terms of microstructure, mechanical properties, capital costs, and energy costs [10].

Before the commercialization of the Castrip process, Broken Hill Proprietary Steel (now BlueScope Steel) and Ishikawajima-Harima Heavy Industries (now IHI Corporation) had a pilot-scale twin roll caster in Australia. The plant was operational from 1990 to 1993 and was successful at producing stainless and low-carbon steel grades [75] before forming Castrip. The aforementioned Baostrip pilot plant has begun trials as well [45]. The specific developments at these locations have not been disclosed but the cooling rates are expectedly very similar to those in the commercialized twin roll casting processes.

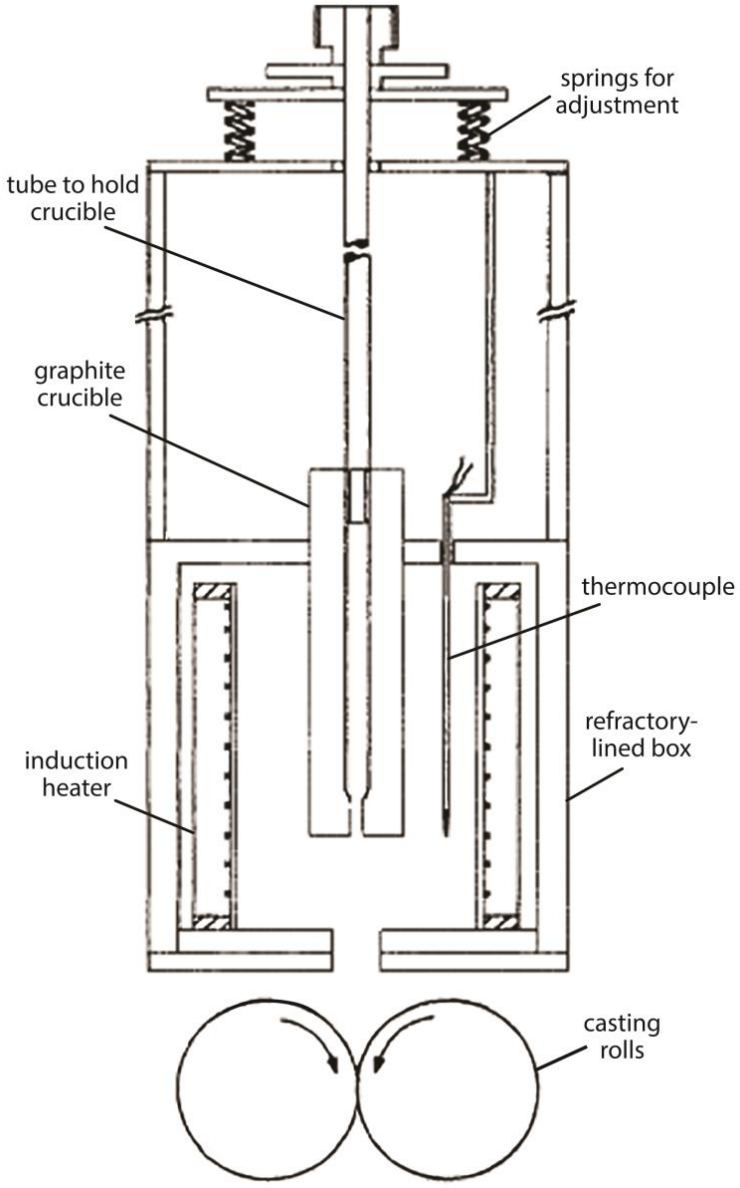

Figure 1.12. A drawing of the lab-scale twin roll caster used by Lakshmikumar et al. [72].

1.1.3.5 Laser surface remelting. Laser surface remelting (LSR) is a small-scale process that allows for precise control of the microstructural growth velocity. The cooling rates across the cross-section of interest can vary from 10^0 to 10^6 K/sec [54]. These variations in cooling rates make it suitable to simulate a variety of solidification processes. The cooling rates across the heat affected zone are usually not measured and

therefore the location influenced by the exact cooling rate is not well-defined. The speed the laser traverses the material can be used to calculate the growth velocity across the melt pool according to Figure 1.13 and Equation 1-4 [76].

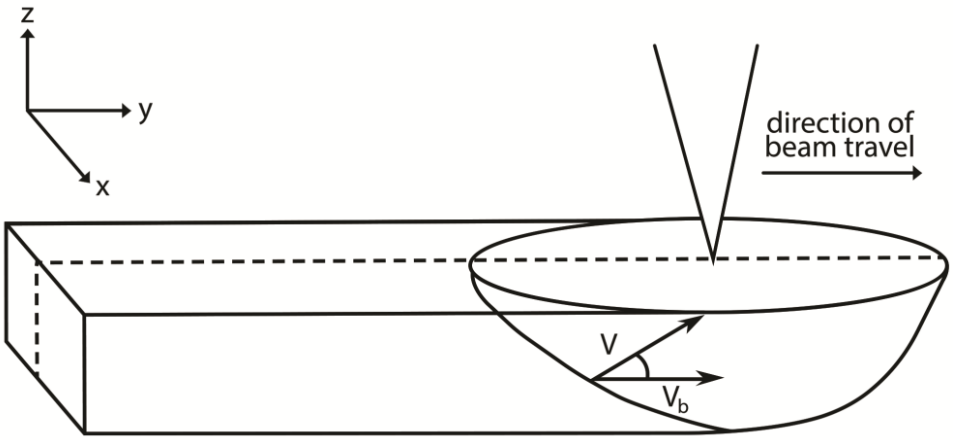

Figure 1.13. A drawing of the LSR process. [76].

$$V = V_b \cos\theta \qquad \text{Eq. 1-4}$$

Where V is the growth velocity, V_b is the laser beam velocity, and θ is the angle between V and V_b, as shown in Figure 1.13.

The growth of these microstructures can be dendritic, cellular, or planar. When the growth is dendritic the growth velocity can be estimated from the PDAS. The general form of the equation for relating the PDAS to the growth velocity is Equation 1-5 [76].

$$\lambda_1 = K_1 \cdot V^{-n} \qquad \text{Eq. 1-5}$$

Where λ_1 is the PDAS, V is the growth velocity, and K_1 and n are experimentally determined values.

One of the benefits of the varied cooling rates is the ability to get a "snapshot" of microstructures from different cooling rates across the heat affected zone. Elmer et al.

studied seven Fe-Ni-Cr alloys and created a phase map corresponding to the various growth velocities as shown in Figure 1.14 [55].

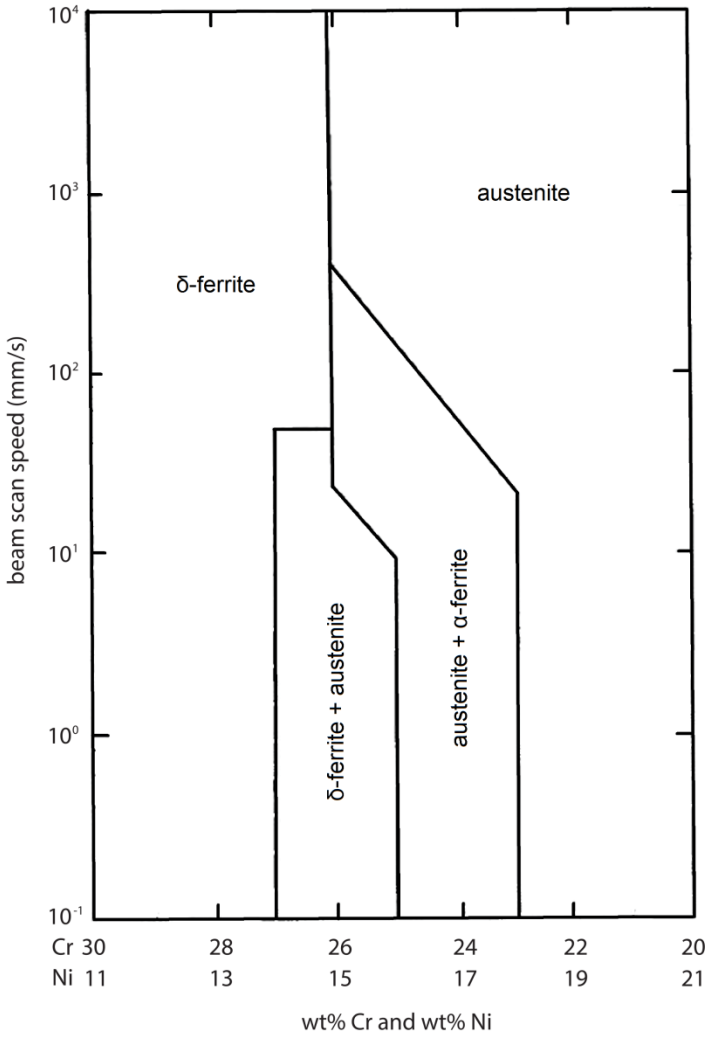

Figure 1.14. A phase map of the primary phases formed during solidification from examination of the microstructures of 7 Fe-Ni-Cr alloys solidified with various growth velocities [55].

Pryds et al. also developed a phase map from their work on Fe-12Cr alloys with varying C contents by conducting LSR experiments and applied the Hunt-Lu model to model the cellular and dendritic growth [76]. In addition the microstructure map they

were able to create, they found the growth mechanism at high carbon contents (above 1.2 wt% C) is purely dendritic whereas it can be cellular and dendritic at lower carbon contents.

Although LSR affords one single view of several cooling rates, the regions are not well-defined and are not of much use past microstructural observations. Their ability to accurately simulate casting conditions is poor as well due to the influence of the material surrounding the weld and the inability to directly quantify the cooling rate.

1.1.3.6 Twin piston quenching and the hammer-anvil method. A slightly higher cooling rate than melt spinning, on the order of 10^5 to 10^7 K/sec, can be achieved through compressing a small amount of molten metal between thermally conductive surfaces in the twin piston quenching (TPQ) and hammer-anvil techniques. The difference between the two processes is that the hammer-anvil method has one moving surface, whereas the TPQ technique utilizes two. The highest cooling rates in the rapid solidification processes examined here come from these techniques. The heat flux can be calculated from thermocouples embedded within the surfaces of each hammer as they are compressed together. One key benefit of these systems is the ability to melt a variety of alloys without concern for alloy contamination. Levitation melting is commonly employed and eliminates the interactions between the melt and refractories and inert atmospheres can be applied to limit the melt-atmosphere interactions.

Pietrokowsky designed the first hammer-anvil apparatus and showed its effectiveness at producing amorphous microstructures in the copper-silver and silver-germanium binary systems [77]. The system was later updated to include a photocell to trigger the rapid movement of the piston as the molten sample drops through the beam of light [25]. A drawing of the updated hammer-anvil apparatus is given in Figure 1.15.

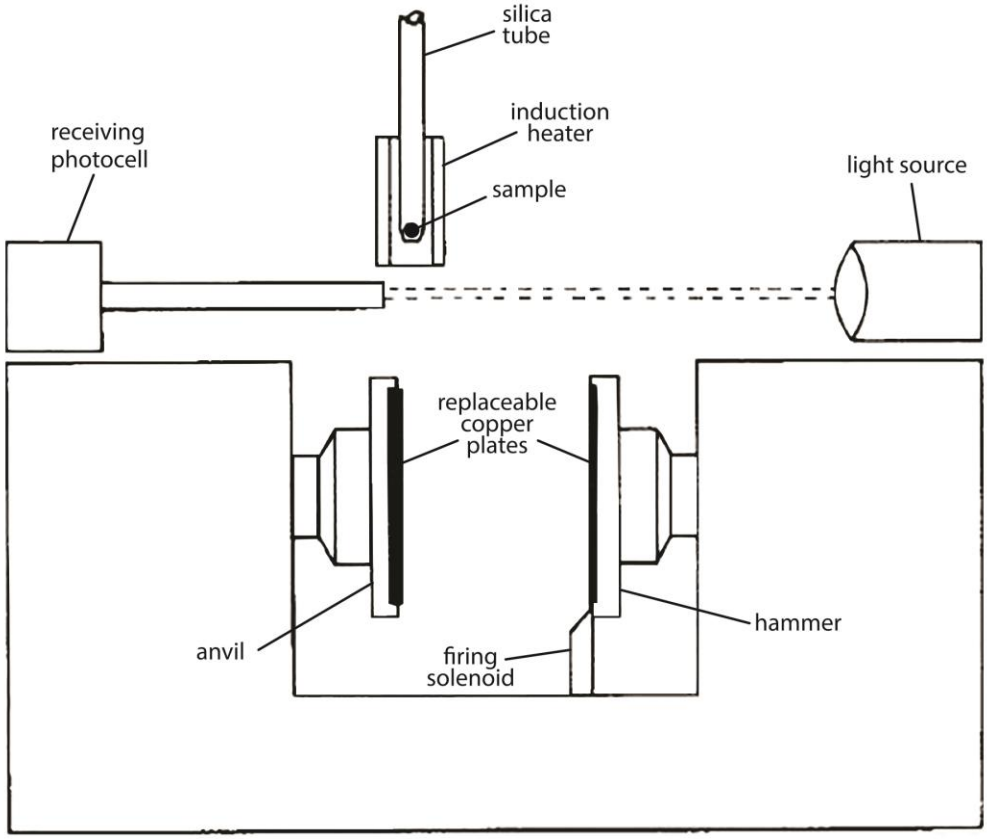

Figure 1.15. A schematic of the hammer-anvil quenching apparatus with a photocell [25].

An important phenomenon in rapidly solidified steels was realized by Hayzelden et al. by using a TPQ device. They surmised the convoluted grain boundaries they saw were a result of dendrites broken down during recalescence [70]. This idea is important for rapid solidification because it implies that although the initial segregation may be negligible, recalescence causes appreciable remelting and drives subsequent segregation. Thus some segregation of solute elements in rapidly solidified samples caused by remelting during recalescence can be expected. This is shown schematically in Figure 1.16. In terms of sample analysis, the heat flux cannot be accurately varied in this process and the samples produced are too thin for any mechanical evaluation.

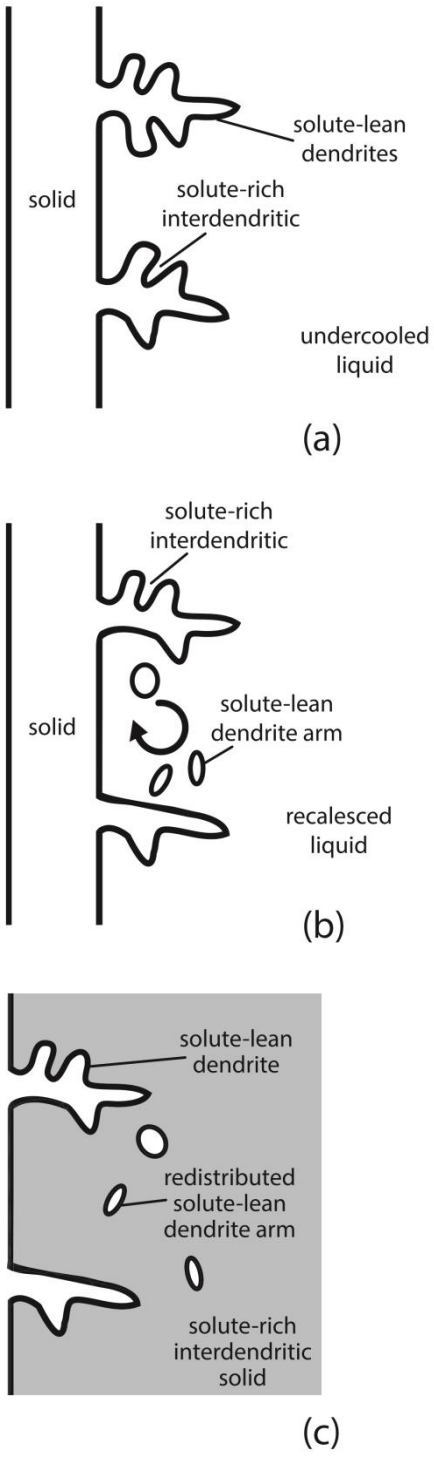

Figure 1.16. Sequence of solute segregation during solidification. (a) Rapid dendritic solidification produces slightly solute-lean dendrites which have a composition very near the slightly solute-rich interdendritic regions. (b) Recalescence causes remelting of the dendrite arms and redistribution of the solute. (c) The final solid is comprised of segregated regions.

1.1.3.7 Melt splat and the gun quenching technique. The melt splat method has been a long-used method for the rapid solidification of alloys. With the addition of a shock tube by Duwez and Willens [78], cooling rates between 10^5-10^7 K/sec have been used to produce samples 1-50 μm thick. The method of melt splat quenching is accomplished through dropping a levitation-melted sample onto a curved or flat copper mold that is either water-cooled or submerged in liquid nitrogen. The shock tube can be used to propel a sample at 150-300 m/sec onto the copper mold with high pressure helium gas [25,78,79]. The apparatus is shown schematically in Figure 1.17.

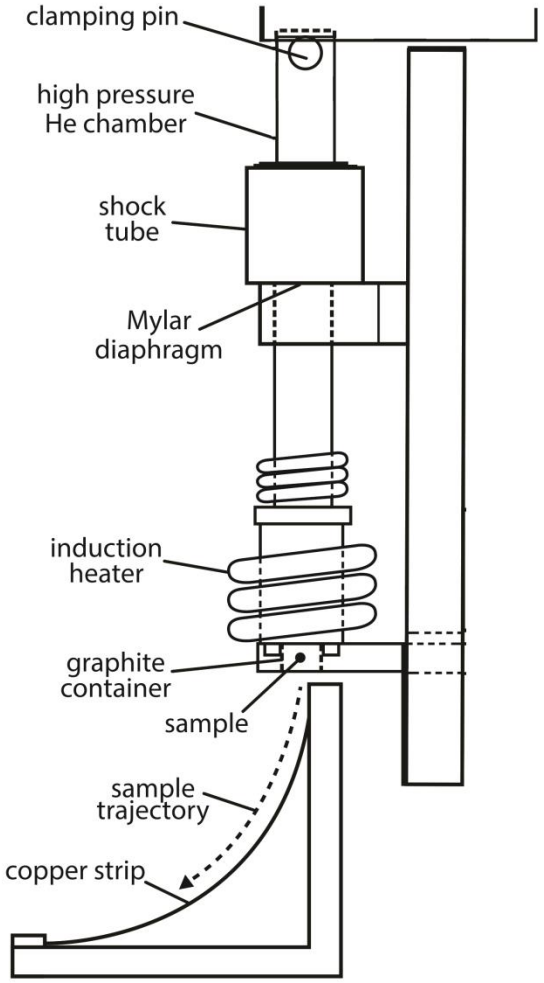

Figure 1.17. A drawing of the gun quenching apparatus used by Duwez and Willens [78].

The samples Duwez and Willens produced were thin enough to be used in the as-cast condition for transmission electron microscopy [25]. Rao used the gun quenching technique to prove metastable and amorphous phases could be produced in the copper-silver system [80].

Wood and Honeycombe proved the solubility of alloying elements can be extended by rapid solidification. Their work of splat quenching Fe-Ni-Cr steels showed the solubility limit of boron in austenite could be increased by 2-3 orders of magnitude [62].

The cooling rate can be changed by adjusting the temperature of the melt and ramp or by varying the pressure with which the melt is ejected.

1.1.3.8 Gas atomization. A variety of cooling rates ranging from 10^2 to 10^5 K/sec can be produced through the gas atomization process [68]. The cooling rate varies exponentially with particle diameter according to Equation 1-6 [67], but cannot be well-controlled through process variables.

$$\dot{T} = B_3 \cdot d^{-m/n} \qquad \text{Eq. 1-6}$$

Where $\dot{T}$ is the cooling rate, d is the particle diameter, and B_3 and the ratio of m/n are determined experimentally.

Obviously there are no direct methods for measuring the temperature change during solidification of the droplets. Therefore, an accompanying method of determining the cooling rate as a function of microstructure, typically SDAS, must be applied. Pryds and Pedersen used a copper wedge mold instrumented with thermocouples to do this [68]. The first patent for a gas atomizing apparatus to produce fine rapidly solidified particles was awarded to Hall in 1924 [81]. Extensive work has been done since 1924 to determine the ideal process parameters for producing metallic droplets in industry. In particular, Mates and Settles focused on the nozzles and the interactions between the solidifying melt and surrounding gas. They found that converging and converging-diverging nozzles performed similarly, and that the particles were smaller as the length of supersonic velocity increased. The secondary breakup of particles became more violent as the supersonic length increased. The supersonic length is also known as the velocity decay

length, and it is the ratio of the velocity decay length to the secondary breakup length which governs the particle size [82,83]. The supersonic length, velocity decay length, and secondary breakup length are shown schematically in Figure 1.18.

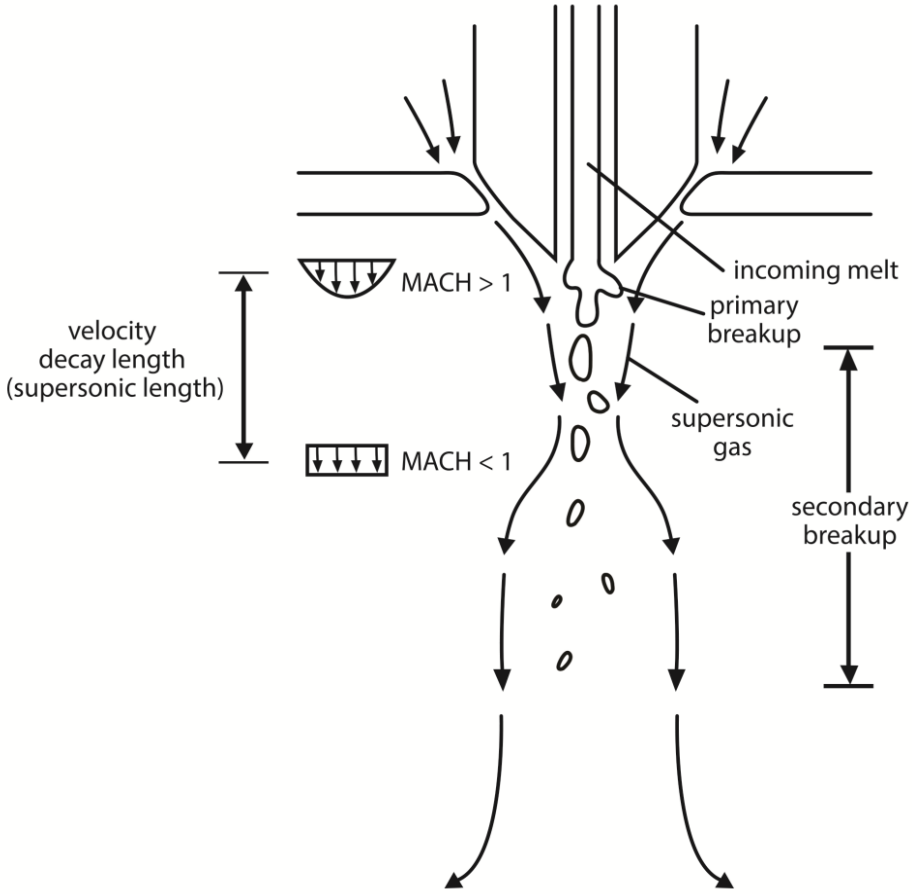

Figure 1.18. A schematic of the gas atomization process.

In the 12Cr-Mo-V martensitic steel Pryds and Pedersen studied, particles below 25-30 μm in diameter contained a dendritic or cellular microstructure of ferrite and austenite. Above 25-30 μm the microstructure consisted of martensite, and was fully martensitic above 60 μm. The critical diameter of 25-30 μm correlated to a critical cooling rate of 48-69x10^3 K/sec. From x-ray diffraction it was determined the smaller particles experienced a delay in the formation of austenite, leading to a lack of martensite [68].

1.1.4. Conclusions. Each lab-scale rapid solidification testing method has its benefits and applications. The type of samples produced and method of measuring the cooling rate for each rapid solidification process is shown in Table 1-2. Lab-scale setups of commercialized processes are understandably the best at simulating casting conditions in terms of generating samples for mechanical testing and the ability to monitor casting parameters. Other laboratory techniques, however, have been effective at simulating various aspects of commercialized DSC processes, such as the initial moments of solidification, the role of the gas layer between the solidifying melt and the substrate, and the effects of changing the casting conditions, without expensive and risky trial heats. Dip testing and melt spinning are the best at controlling the casting conditions to yield solidification rates present in industry.

Alloys containing increased amounts of Mn (5-15 wt%), C (0.1-0.3 wt%), and other alloying elements such as Al, Si, and Cu have the most promise on the path of alloy development to achieve 3rd generation properties. However, as detailed above, they are not without their casting and post-processing difficulties.

Table 1-2. References to the studies, the sample sizes produced, and the method of temperature measurement for the rapid solidification processes examined in this work.

Rapid Solidification Process and [References]	**Sample Size**	**Direct Measurement of Cooling Rate**
Dip Testing [56,59-61,63,64]	0.5-1 mm thick strip	Embedded thermocouples
Melt Spinning [65-70]	20 μm thick strip	Pyrometer
Lab-Scale horizontal single belt casting [71,72]	3 mm thick strip	Embedded thermocouples
Lab-Scale twin roll casting [10,19,45,73-75]	5-100 μm thick strip	Possible by pyrometer
Laser Surface Remelting [55,76]	Varying widths and depths of weld pool	Possible by thermocouples
TPQ/Hammer-Anvil [25,70,77]	30-75 μm thick disks with 25 mm diameter	Embedded thermocouples
Melt-Splat/Gun Quenching [25,62,78-80]	1-50 μm thick uneven strip	Possible by pyrometer
Gas Atomization [68,81-83]	5-600 μm diameter spherical particles	Possible by pyrometer

1.2. MOTIVATION FOR THIS WORK

The development of 3rd generation steel alloys and insight into their casting and processing is of paramount importance to the steel industry. Literature showed that dip testing is the most efficient lab-scale testing method in terms of space requirements, cost, applications of the samples produced, generation of quantitative data, and applications to industrial DSC processes. The literature also showed that variations of the alloying elements in alloys containing 5-15 wt% Mn and 0.1-0.3 wt% C alloys are a promising direction for alloy development to meet the 3rd generation AHSS requirements. For these reasons, a dip testing apparatus was designed and built to examine the microstructural characteristics of many potential 3rd generation alloys which potentially exhibit dual TRIP by the $\gamma \rightarrow \varepsilon \rightarrow \alpha'$ transformation under rapid solidification conditions. It was hypothesized, based on the review presented, that casting by DSC will yield a better final product without the casting difficulties associated with producing these alloys by conventional TSC.

2. EXPERIMENTAL PROCEDURE

2.1. DIP TESTING

An apparatus to approximate the solidification rates present in twin roll casting was first used by Strezov and Herbertson in their studies on the initial heat transfer during solidification of 304 stainless steel at Broken Hill Proprietary Steel (now BlueScope Steel and one of the three member companies of Castrip) in Australia [59]. Since then, other systems have been developed to simulate horizontal single belt casting (see Section 1.1.3.3) in addition to further development of dip testing (see Section 1.1.3.1). A dip testing apparatus was designed and built at Missouri S&T as a method of evaluating the casting and microstructural characteristics of potential 3rd generation AHSS under rapid solidification conditions.

The design and build of the dip tester at Missouri S&T was done in close cooperation with Castrip employees who had experience with the dip tester at BlueScope Steel in Australia whose contact information is listed in the Appendix. The Appendix also contains a user manual for the operation of the dip tester. Their experience provided an outline for the design; however some details had to be changed. The dip tester at Missouri S&T is shown in Figure 2.1.

The goal of dip testing is to produce cooling rates similar to those present in twin roll casting. These cooling rates yield the microstructures expected to be present in steel produced by twin roll casting. This is done by rapidly dipping a steel paddle containing textured and chrome-coated copper blocks in a steel melt. The copper blocks were manufactured from the surface of the casting rolls used in the Castrip process. The time vs. distance from the melt surface profile was prepared to be most near the path of steel through the casting rolls in a twin roll casting and is shown in Figure 2.2. The distance from the melt surface vs. velocity profile is in Figure 2.3. The steel paddle spends approximately 0.4 seconds in the melt and the copper blocks are immersed for approximately 0.2 seconds when the dip is performed at 60 m/min.

Figure 2.1. Dip tester setup. 1: 200 lb induction furnace, 2: furnace lid, 3: dipping paddle with textured copper blocks, 4: servo motor enclosure, 5: melt-sensing circuit's power supply and voltmeter, and 6: dip tester electronics enclosure.

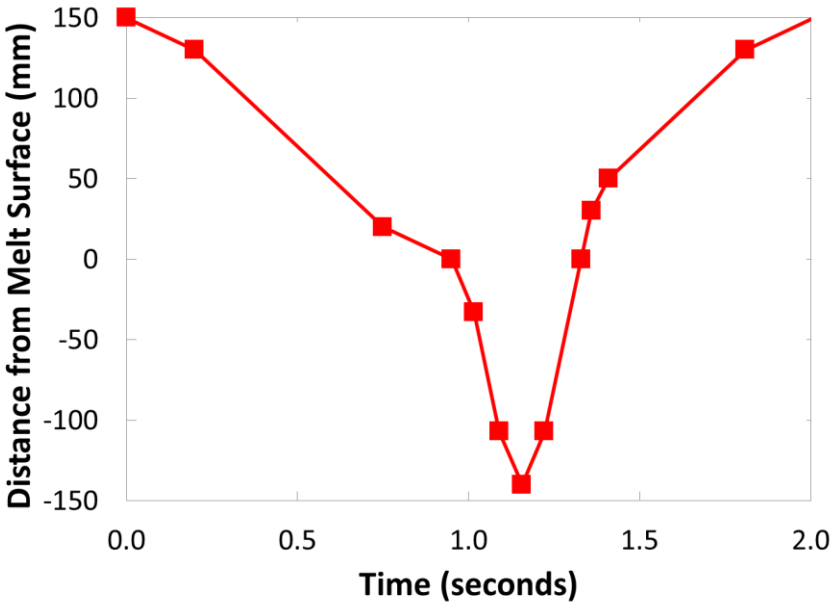

Figure 2.2. The targeted time vs. distance of the bottom of the paddle from the melt surface dipping profile at a dipping speed of 60 m/min.

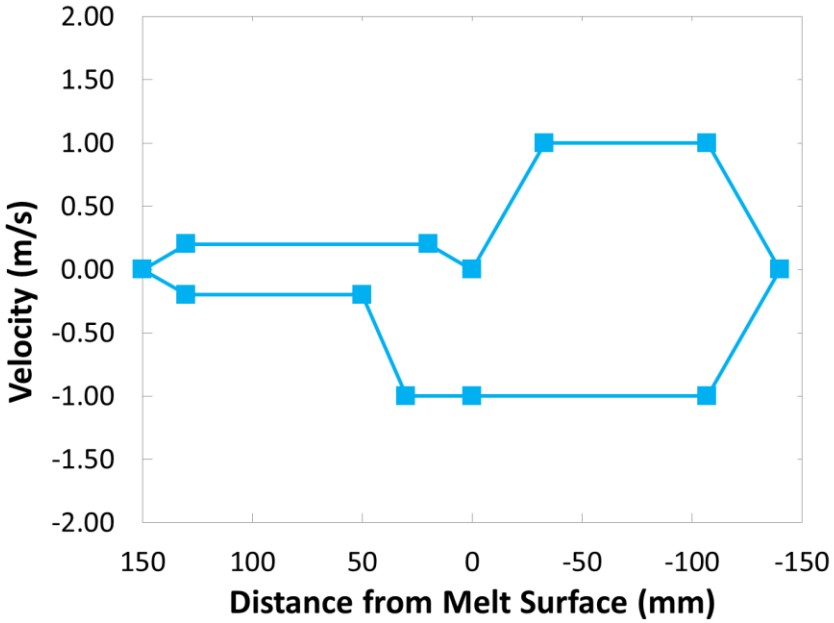

Figure 2.3. The distance from melt surface vs. velocity profile at a dipping speed of 60 m/min.

A circuit, utilizing a solid state relay, was incorporated into the electronics assembly to sense the surface of the melt and initiate the dipping sequence. The solid state relay sends a signal to the programmable logic controller (PLC) when the melt-sensing wires touch the surface of the melt and complete the circuit. The PLC receives the signal and initiates the dipping sequence.

T-type thermocouples in the copper blocks send millivolt signals to the transmitters on the back of the dip test servo motor enclosure. The position of the T-type thermocouple wires in the blocks was varied during initial heats to find an attachment configuration that gave the best response to the temperature increase.

Initially the negative, or constantan, wire was first screwed into the back of the block at a precise 4.00 mm distance from the surface of the blocks. The positive, copper, wire was secured to the back surface of the block. Since the block is a Cu-Be alloy, it was assumed the conductivity through the block would be very similar to the wire. During testing this thermocouple configuration produced a delayed signal.

The arrangement of the thermocouples was then adjusted so both wires were screwed down at the 4.00 mm distance from the surface of the blocks. The signal was

more responsive to abrupt changes during the testing but was somewhat prone to small differences between the two blocks. These changes towards optimizing the system gave heat fluxes which were not consistent across the field of alloys tested. Therefore, the heat flux values cannot necessarily be directly compared from alloy to alloy. When appropriate, the k-factor, defined in Equation 1-1, was instead used to compare selected alloys.

Thermocouple transmitters linearize and amplify the millivolt signals to voltage signals between 0 to 10 VDC to increase the resolution of the measurements. Therefore each volt sent by the transmitters is equal to 40°C. The transmitters send the amplified and linearized signals to the NI USB-6009 which samples at 2017 Hz. This sampling rate was selected to avoid interference with other electrical components in the foundry. A macro within a temperature data acquisition (DAQ) Excel Workbook gathers the data and converts the voltages to temperatures and plots the data. From this data it is possible to see the sharp increase in temperature as the copper blocks entered the melt and record the temperature rise during the time the blocks were immersed as shown in Figure 2.4. The temperature increase and time spent in the melt are input into a spreadsheet to calculate the heat flux via an inverse heat conduction equation developed by BlueScope Steel. The equation and associated coefficients for thermocouple distances between 4.0-4.3 mm from the surface of the copper blocks is shown in Equations 2-1 and 2-2 and Table 2-1. The coefficients were calculated from industrial tests where the temperature rise across embedded thermocouples was related to a known heat flux.

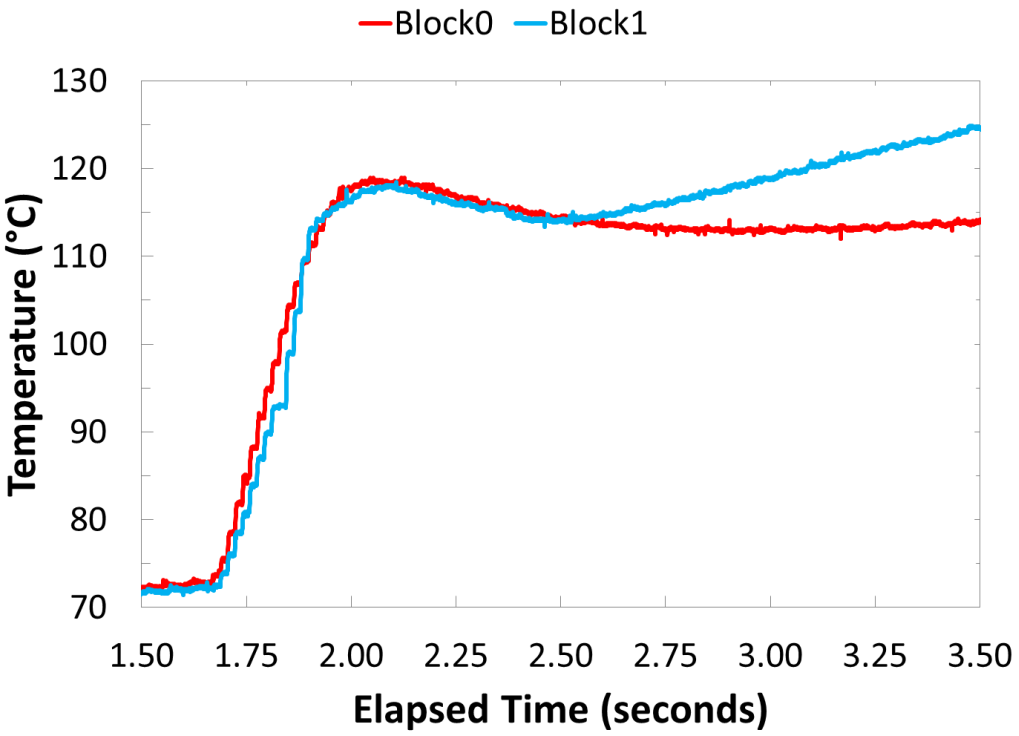

Figure 2.4. A plot of the temperature rise during a dip.

$$\bar{Q} = \frac{\Delta T_{actual}}{\Delta T_{calc}} (10\, {}^{MW}/_{m^2}) \qquad \text{Eq. 2-1}$$

Where $\bar{Q}$ is the average heat flux, ΔT_{actual} is the measured temperature rise, $10\, {}^{MW}/_{m^2}$ comes from the known heat flux in the inverse heat conduction calculation, and ΔT_{calc} is given in Equation 2-2.

$$\Delta T_{calc} = at^6 + bt^5 + ct^4 + dt^3 + et^2 + ft + g \qquad \text{Eq. 2-2}$$

Where t is the time the blocks spent in the melt and a, b, c, d, e, f, and g are constants dependent upon the distance of the thermocouple from the surface of the copper blocks and are provided in Table 2-1. The constants were calculated during the same study as the inverse heat conduction calculations.

Table 2-1. Coefficients for Equation 2-2 as a function of the distance of the thermocouples from the surface of the copper blocks.

Thermocouple Distance from Surface (mm)	Coefficients in Equation 2-2						
	a	b	c	d	e	f	g
4.0	234,253	-321,253	173,915	-46,841	6,248.8	3.208	-0.607
4.1	226,124	-311,262	169,402	-45,998	6,227.7	-12.434	-0.488
4.2	217,333	-300,330	164,358	-45,003	6,183.9	-26.443	-0.375
4.3	208,049	-288,696	158,911	-43,889	6,121	-38.938	0.27

The DAQ program for controlling the location of the paddle at a given time was developed at Missouri Tooling and Automation. The servo motor and servo motor drive relay information approximately 1 million times per second. To pass this information to the PLC and extract it would take an immense amount of time even at the rapid rates of data transfer through the Ethernet wire. The actual location of the servo at each 3 millisecond interval is recorded instead. It is possible to extract the command position vs. actual position data from the PLC but the process requires more time and is not typically done during a heat. This data is compared to the target velocity profile periodically to ensure the servo motor has not lost accuracy. An example of the command, or target, position vs. the actual position is shown in Figure 2.5. This data is useful since the goal of dip testing is to maintain a velocity profile in the melt near that of steel passing through the rolls of a twin roll casting. Deviations in the position of the servo can yield erroneous results.

One of the benefits of this lab-scale method is that the composition of the melts, and therefore samples, can be adjusted during one heat. This is one of the advantages of dip testing over a lab-scale twin roll caster. This is done by using a calculated charge table to make adjustments prior to each heat. After each sample is taken, pure alloys or ferro-alloys are added to the melt and the next composition can be tested. The recovery of alloying additions is continuously updated within the charge table after analyzing the chemistry from each sample after the heat to achieve accurate compositions. It should be noted the other alloying elements needed slight additions as well when the increases in alloy contents were significant (about 1% or greater). The initial melt weight was selected so the final melt weight was always less than 180 lbs.

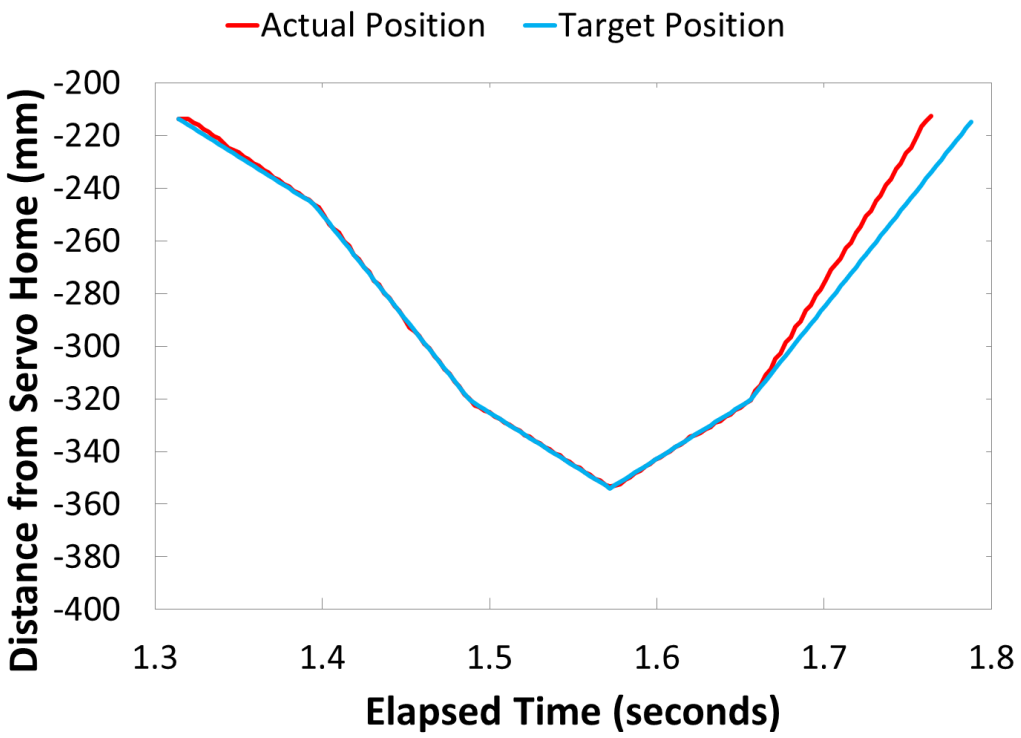

Figure 2.5. The target and actual velocity profiles as downloaded from the servo motor drive and PLC.

The samples produced by dip testing can be used for a variety of tests. In the past and in this work, they have been used for optical microscopy, scanning electron microscope (SEM) evaluation, x-ray diffraction (XRD), microhardness, evaluation of the sample surface quality, heat transfer analysis, and other tests currently under development such as a shear punch method [84,85]. Another comparison can be made by testing an alloy currently produced by the twin roll casting process and evaluate the characteristics associated with its performance under dip testing conditions. This aids in the overall analysis of other developmental alloys when a comparison can be made to an alloy known to be castable by the twin roll casting process.

2.2. POTENTIAL FOR FRACTIONAL SOLIDIFICATION

There is the potential for fractional solidification to occur during dip testing. Fractional solidification can take place when samples are rapidly cooled and removed from a bulk material. The undercooling that occurs when the sample is removed leads to

solute segregation, and the sample chemistry is different than the chemistry of the bulk material. In addition, the chemistry of the near-interface liquid becomes rich in solute because the samples being taken are lean in solute. This concept is shown when evaluating a binary phase diagram such as the Fe-C phase diagram in Figure 2.6.

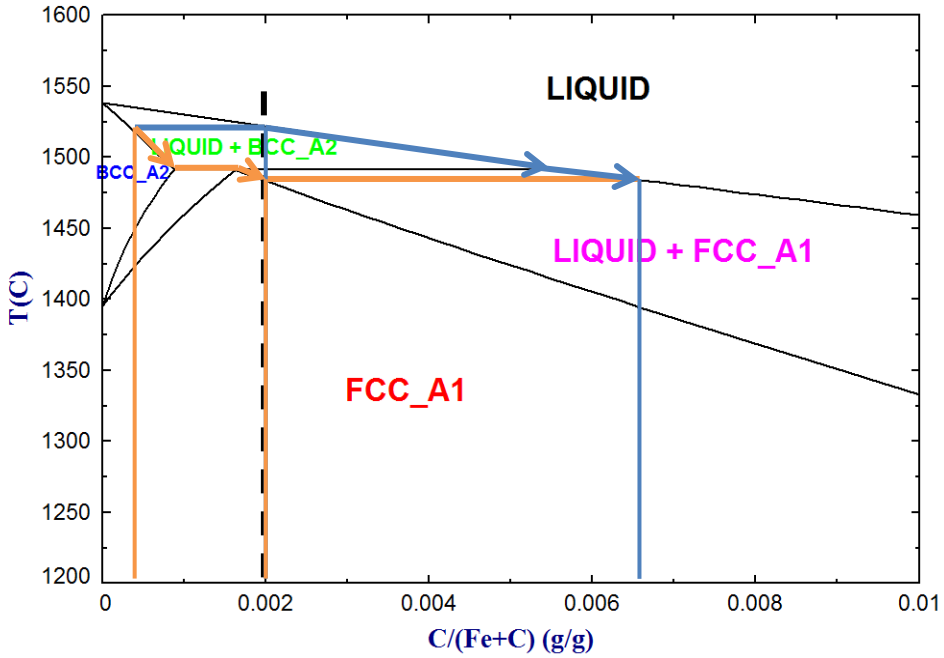

Figure 2.6. Fe-C phase diagram with the equilibrium solidification path of 0.2 wt% C shown.

An alloy of 0.2 wt% C solidifies on the path shown. By equilibrium solidification, the initial solid, δ-ferrite, contains 0.03 wt% C while the remaining liquid just past the liquidus contains 0.21 wt% C, as shown by the orange path. Just above the solidus the solid, austenite, contains 0.20 wt% C and the last liquid contains 0.67 wt% C, as shown by the blue path.

Scheil modeling is occasionally used during solidification calculations passing through the peritectic region to simulate the opposite extreme case of solidification where there is no diffusion in the solid. This is done because δ-ferrite is the first solid phase to form, with austenite forming around it. The tightly packed structure of austenite slows the diffusion of carbon from the liquid to the δ-ferrite. It predicted carbon contents of the

liquid and δ-ferrite just below the liquidus temperature of 0.2 wt% and 0.03 wt%, respectively. Scheil modeling showed that full solidification occurred at about 1150°C where the remaining liquid passes through the eutectic. Actual solidification is a combination of the two theories. The carbon contents at a temperature just above the equilibrium solidus were calculated. The final liquid contained 0.64 wt% C, the solidified δ-ferrite contained 0.05 wt% C, and the austenite contained 0.19 wt% C. The differences in the amount of each phase present during equilibrium and Scheil solidification are shown in Figures 2.7 and 2.8.

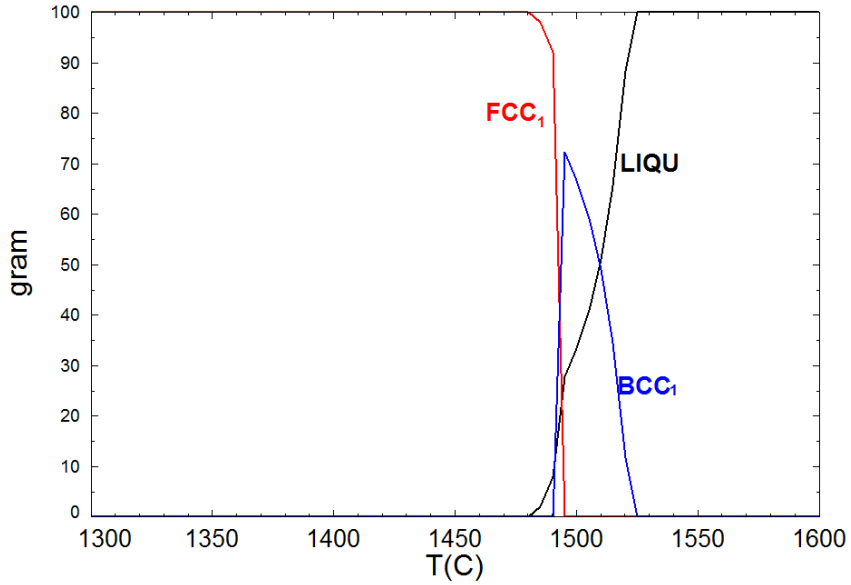

Figure 2.7. Amount of liquid (LIQU), δ-ferrite (BCC_1), and austenite (FCC_1) present during equilibrium solidification, as calculated with FactSage.

Both solidification methods show the initial solid removed from the melt contains a carbon content much lower than the bulk carbon content. Continually removing the solute-lean samples produces a solute-rich melt. This concept has been exploited, albeit by using some different methods, to refine partially solidified solutions [86-88]. However, the conditions for fractional solidification require a growth front that allows for the diffusion of solute back into the bulk melt. This growth front is typically either planar or results from amorphous solidification. Dendritic solidification allows for diffusion

perpendicular to the growth front and traps solute-rich liquid in the regions between the dendrites. Samples solidified with dendritic growth maintain the bulk composition by an average of the solute-lean dendrites and solute-rich interdendritic region. All of the microstructures in the dip test samples were dendritic. Figure 2.9 shows the dendritic growth across the sample in an un-etched micrograph from Alloy 5.2.

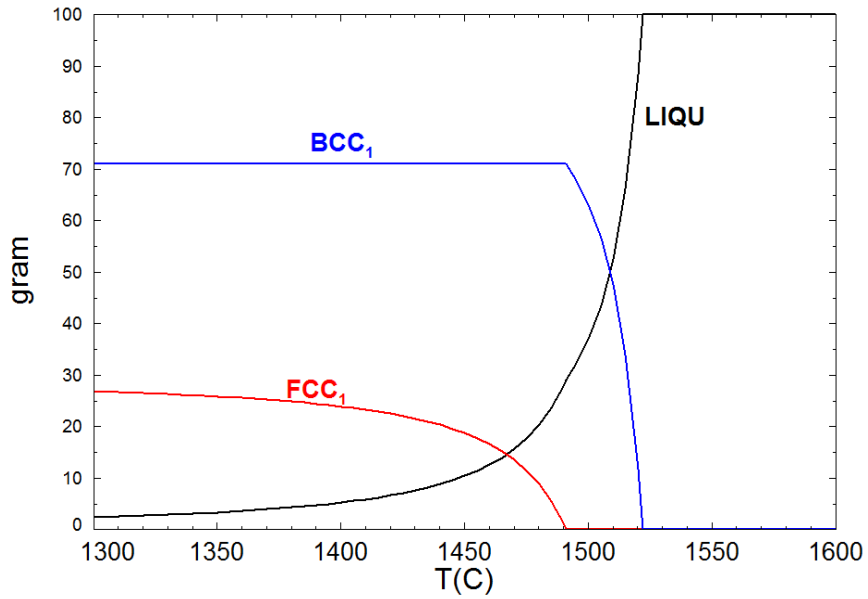

Figure 2.8. Amount of liquid (LIQU), δ-ferrite (BCC_1), and austenite (FCC_1) present during Scheil solidification, as calculated with FactSage.

The carbon content in an immersion sample taken from the bulk melt was compared to a sample taken by dip testing to verify if the compositions were the same. The carbon contents were compared because calculations showed that the carbon content of a dip test sample would be approximately 0.06 wt% when taken from a steel melt with a bulk carbon content of 0.2 wt%. Experimentally, LECO carbon analysis showed both samples had carbon contents of 0.18 wt%. The identical carbon contents and dendritic growth are evidence that fractional solidification is not occurring during dip testing.

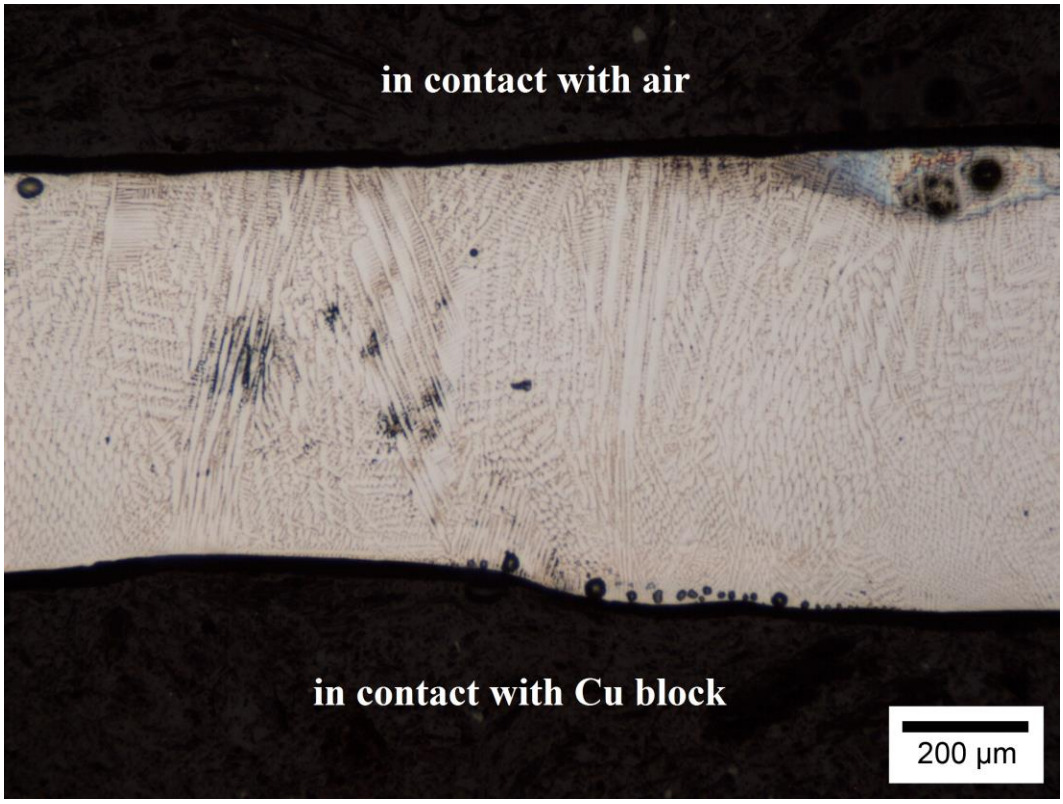

Figure 2.9. Dendritic growth across a sample from Alloy 5.2.

2.3. HEAT PROCEDURES

Several heats were prepared for the testing and analysis of various 3rd generation AHSS alloys. The alloys and their compositions, as measured by arc spectrometry, LECO carbon and sulfur, and LECO oxygen and nitrogen, are provided in Table 2-2. The alloy designations provided in Table 2-2 will be used to describe each of the alloys in the Results and Discussion section, Section 3.

Table 2-2. Compositions, dipping superheats, and dipping speeds of the alloys tested.

Alloy	wt% C	wt% Mn	wt% Si	wt% Al	wt% Cu	Dipping Superheat (°C)	Measured Liquidus (°C)	Dipping Speed (m/min)
1-1	0.21	3.3	0.3			102	1500	60
1-2	0.22	3.3	0.3			103		60
1-3	0.33	3.3	0.3			110		60
1-4	0.32	4.4	0.3			122		60
1-5	0.31	5.5	0.3			111		60
1-6	0.31	6.5	0.3			123	1480	60
2A-1	0.24	3.4	0			117	1500	60
2A-2	0.24	3.4	0.6			84		60
2A-3	0.23	3.5	1			104		60
2A-4	0.23	3.4	1.5			122		60
2A-5	0.22	3.6	1.8			120		60
2A-6	0.22	3.4	2.2			104	1472	60
2B-1	0.31	4.9	0			90	1487	60
2B-2	0.31	5.1	0.5			96		60
2B-3	0.31	5.2	1.2			101		60
2B-4	0.3	5.2	1.5			98		60
2B-5	0.3	5.3	2.1			101		60
2B-6	0.3	5.2	3			102	1456	60
2C-1	0.22	7.7	0			106	1483	60
2C-2	0.22	7.9	0.5			114		60
2C-3	0.22	7.9	1			138		60
2C-4	0.22	7.9	1.5			130		60
2C-5	0.22	7.9	2			129		60
2C-6	0.22	7.9	2.3			117	1453	60
5-1	0.16	14.3	3	0.9		69	1422	60
5-1	0.16	14.3	3	0.9		74		60

Table 2-2. Compositions, dipping superheats, and dipping speeds of the alloys tested (cont.).

Alloy	wt% C	wt% Mn	wt% Si	wt% Al	wt% Cu	Dipping Superheat (°C)	Measured Liquidus (°C)	Dipping Speed (m/min)
5.2-1	0.18	12.9	0.1	0		94	1464	60
5.2-2	0.18	13	1.1	0		102		60
5.2-3	0.18	13.3	2	0		96		60
5.2-4	0.17	13.1	2.9	0		109		60
5.2-5	0.17	12.8	3	0.6		109		60
5.2-6	0.17	13	3	1.4		107	1413	60
7-1	0.1	10.4	2.8	0.2		101	1447	60
7-2	0.17	10	2.8	0.2		99		60
7-3	0.18	11.5	2.7	0.1		98		60
7-4	0.18	17.1	2.7	0.1		101		60
7-5	0.19	19.6	2.7	0		99		60
7-6	0.17	17.9	2.7	1.2		105	1412	60
P-2	0.11	7.8	2	0.8		91	1466	60
P-3	0.11	7.8	2	0.8		99		60
P-4	0.12	7.9	3.1	0.7		101		60
AC-1	0.2	7.5	2.5		2	106	1440	30
AC-2	0.2	7.5	2.5		2	101		60
AC-3	0.2	7.5	2.5		2	104		48
AC-4	0.2	7.5	2.5		2	107		72
AC-5	0.2	7.5	2.5		2	65		60
AC-6	0.2	7.5	2.5		2	64		72
AC-7	0.18	7.4	2.5		2	128		60
AC-8	0.18	7.4	2.5		2	145		72
AC-9	0.18	7.4	2.5		2	148		48
C-1	0.21	0.6	2.4	0		99	1480	60
C-2	0.21	0.6	2.4	0		94		60

Table 2-2. Compositions, dipping superheats, and dipping speeds of the alloys tested (cont.).

Alloy	wt% C	wt% Mn	wt% Si	wt% Al	wt% Cu	Dipping Superheat (°C)	Measured Liquidus (°C)	Dipping Speed (m/min)
C-3	0.23	0.6	2.4	0.6		89		60
C-4	0.23	0.6	2.4	0.6		87		60
C-5	0.24	0.6	2.4	1.2		80		60
C-6	0.24	0.6	2.4	1.2		82		60
C-7	0.25	0.6	2.5	1.9		98		60
C-8	0.25	0.6	2.5	1.9		79		60
C-9	0.26	0.6	2.5	2.6		78		60
C-10	0.26	0.6	2.5	2.6		94	1500	60

The alloys listed in Table 2-2 were prepared using various combinations of induction iron, graphite, electrolytic Mn, pure Al, pure Cu, and Fe75%Si. The same charge material was used to make changes in the alloy composition during various heats. The alloy additions were made by vigorous mixing into the melt. The recoveries were continually updated to achieve compositions as close to the target compositions as possible. Once all of the charge had melted, the melt was calcium treated with steel-sheathed Ca powder through a synthetic calcium-aluminate slag which was added to the surface of the melt. The melt was then de-slagged using a vermiculite slag flux.

The targeted superheats were calculated from FactSage predictions and experience from previous experiments with these alloys. S-type thermal analysis cups were poured with the first and last compositions of each dip test to determine the liquidus temperatures. The results are shown in Table 2-2. The superheat at which each sample was taken was kept as consistent as possible. Typical superheats were between 80-150°C, depending on the design of the test. If the superheat was not varied as part of the design of the experiment, the targeted superheat was 100°C. This was done because previous tests showed a difference in the sample quality when the superheat was varied significantly. It was occasionally desirable to vary the superheat within a dip test heat to

determine the optimum superheat that yielded the highest heat flux. The actual superheats are provided in Table 2-2. The dipping speed was also occasionally varied to determine the effect of dipping speed on the heat flux. When the dipping speed was not a selected variable in the design of the experiment, it was kept constant at 1.0 m/sec. The actual dipping speeds are provided in Table 2-2 as well.

Samples were taken from the melt by two methods. First, the dip tester was used to remove a thin, approximately 0.6-1 mm sample. Dip test samples from Alloy 7 are shown in Figure 2.10. The details of the dip test sample procedure were described previously in Section 2.1 and additional information is provided in the Appendix. One or two immersion samples were taken within a minute following the dip test using a Heraeus Electro-Nite SAF 120 steel immersion sampler. These samples were used to check the composition. A sample is shown in Figure 2.11. The measured cooling rate of the dip test samples was 10^3 K/sec. The cooling rate of the immersion samples was approximated as 10^2 K/sec from a comparison of the SDAS from the known cooling rates of the dip test samples.

After the immersion sample was taken following the dip test, charge additions to adjust the chemistry were added, changes in the superheat or dipping speed were made, and the chrome-coated copper blocks were brushed with a brass wire brush. The blocks were brushed so that any effect the oxide layer formed on the blocks would be minimal, and the only changes in the heat flux would be from the controlled variables. Literature showed [89] that as the oxide layer was allowed to continually form, the peak heat flux could be increased by more than four times. If necessary, the melt was de-slagged with a vermiculite slag flux. De-slagging was critical with the alloys high in aluminum because the melt became very drossy and the dross affected the heat flux and sample quality. Twin roll casting of these alloys would pull in minimal amounts of dross because the bottom of the melt, which is cleaner, passes through the casting rolls.

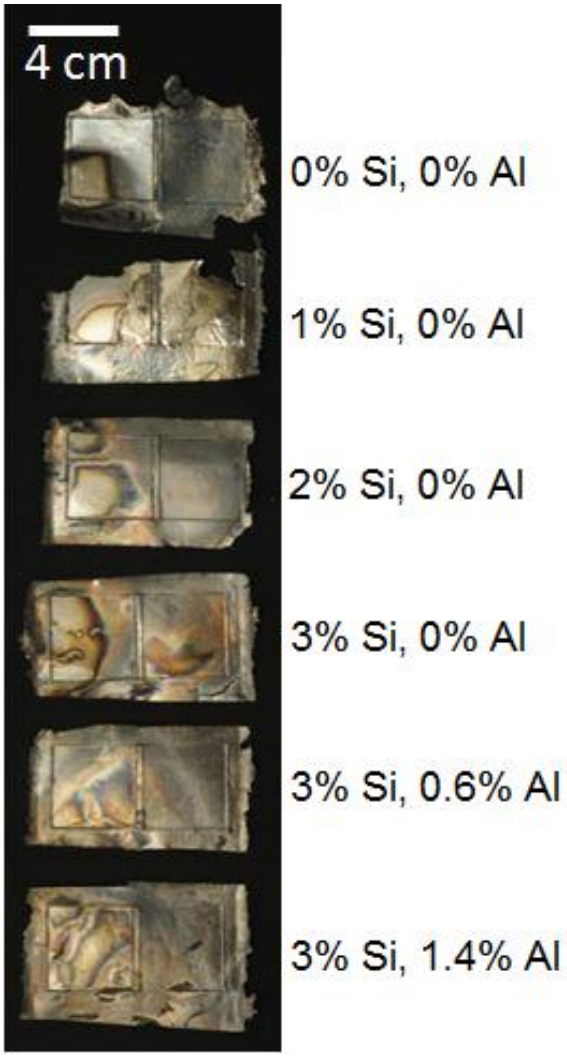

Figure 2.10. Samples generated from the dips at the 6 compositions of Alloy 7.

Figure 2.11. An immersion sample taken from the melt.

2.4. TESTING AND ANALYSIS PROCEDURES

Chemical analysis was done using an Oxford Foundry-Master UV arc spectrometer. Multiple standards above and below the target elemental composition were tested, and then the equation from a best-fit line was used to improve the accuracy of the analysis for the elements of interest. A LECO CS600 was used to measure the carbon and sulfur contents, and a LECO TC500 was used to measure the total oxygen and nitrogen contents.

Samples for optical examination were metallographically sectioned with a slow speed wet abrasive saw, mounted in bakelite, and prepared for optical examination by standard metallographic techniques. Vibratory polishing using 0.03 μm colloidal silica media was used as the final polishing step. The SDAS were taken as averages of the measurement across 30 secondary dendrite arms in the un-etched micrographs. These measurements were then used to calculate the total average SDAS for each sample. Equations 2-3 and 2-4 are provided for a more clarification on how the average SDAS were calculated.

$$SDAS_{i,j} = \frac{d_j}{N_j} \qquad \text{Eq. 2-3}$$

Where $SDAS_{i,j}$ is the average SDAS for the particular measurement across the secondary dendrite arms of interest, j, in each sample, i. d_j is the distance across the secondary dendrite arms of interest and N_j is the number of dendrite arms in the measurement.

$$SDAS_i = \frac{\sum N_j * SDAS_{i,j}}{\sum N_j} \qquad \text{Eq. 2-4}$$

Where $SDAS_i$ is the weighted average SDAS in the sample.

The thicknesses of the samples were measured using an optical microscope at low magnification. The thickness for each sample was taken as the average of 8 or more measurements across the middle of the sample. The time in the melt was found by examining the velocity data from the PLC. The k-factor was then calculated using

Equation 1-1. When shown, the error bars on the k-factor represent variability in the thickness of the samples.

The Cr-coated copper blocks were prepared for analysis in an ASPEX SEM/EDS by washing in ethanol and blowing off any dust with a compressed air can. Energy dispersive spectroscopy (EDS) was used to characterize the oxide layer formed on the surface of the Cr-coated copper blocks. Images were taken with the backscattered electron detector since the system was not equipped with a secondary detector. EDS mapping of the surface oxide was done by averaging 2 frames of a 256 x 256 image with a scan rate of 10 ms/pixel.

ANSYS Fluent fluid dynamic modeling software was used to simulate various parameters during dip testing. The primary parameter examined was the effect of an air gap between the solidifying shell and the copper substrate on the heat flux and sample thickness. From varying the air gap, the thickness of the sample during the test time, the average heat flux, and the temperature rise were all calculated as a function of the thickness of the air gap. The average initial temperature of the solidifying melt was assumed to be 1540°C, for a superheat of 100°C.

The FSstel and FToxid databases of FactSage 6.4 thermodynamic software were used for the thermodynamic calculations. Within FactSage 6.4, the Phase Diagram, Equilib, and Reaction modules were used for various portions of analysis.

3. RESULTS AND DISCUSSION

3.1. COMPARISON TO CURRENT CASTRIP ALLOYS AND OTHER WORK

With the idea of exploiting a twin roll casting process to produce 3rd generation AHSS alloys, comparisons to the compositions of the alloys produced daily at Castrip in Crawfordsville, IN were made to the 3rd generation alloys tested here. In addition, the newly built dip tester needed to be benchmarked against other systems. This was done by searching literature to find typical setups during dip testing and analyzing the resulting data.

3.1.1. Comparison to Current Castrip Grades. The material Castrip casts on a routine basis are low carbon grades (<0.035 wt% C), with 0.4-1 wt% Mn and 0.2-0.3 wt% Si [54]. The developmental martensitic and quench and partition grades Castrip has cast fall in the ranges of 0.2-0.35 wt% C, 0.3-2% Si, and 0.5-3 wt% Mn [54]. These grades are comparable to Alloys 1-1, 1-2, 1-3, 2A-1, 2A-2, 2A-3, 2A-4, C-1, and C-2 in this work. These alloys were successfully dip tested and will be referred to in later discussions on the effects of alloying elements in these alloys.

The peak heat fluxes from the experimental dip tests are shown in Figure 3.1. The alloys that are similar to those cast at Castrip (Alloys 1-1, 1-2, 1-3, 2A-1, 2A-2, 2A-3, 2A-4, C-1, and C-2) yielded peak heat fluxes between 5-12 MW/m^2. This range of heat fluxes is slightly lower than the typical peak heat fluxes present in the Castrip process of 13-16 MW/m^2 [90]. This is to be expected for the developmental grades during dip testing. The Castrip process also presses the two solidifying shells together so the heat must be transferred through the copper rolls in contact with the strip. Heat cannot be transferred to the ambient air, as it can during the dip test. Therefore, reasonable agreement can be seen between dip testing and the process it is meant to simulate, i.e. the twin roll casting process of Castrip. Additionally the thicknesses of the samples give insight into how the alloys would cast. The solidified strip out of the casting rolls is typically between 1.6-2 mm thick. Sample thicknesses 0.5-0.7 mm thick represent approximately half of the strip solidified in the Castrip process. The remaining thickness can be attributed to a small amount of remaining liquid passing through and solidifying after the roll nip, as shown in Figure 3.2.

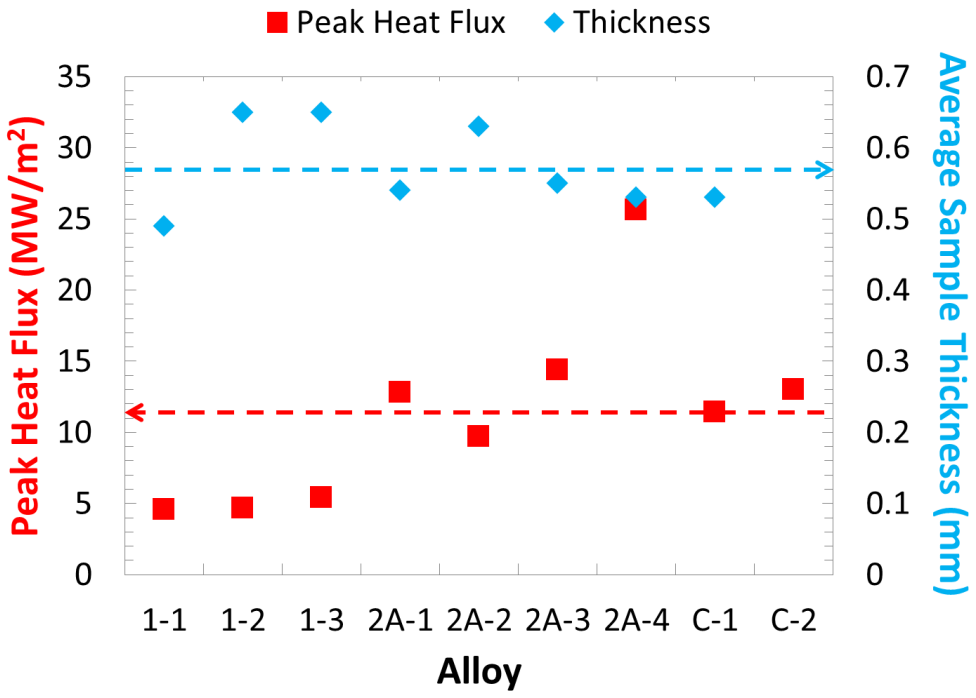

Figure 3.1. Heat flux and sample thickness for the alloys similar to the Castrip development grades. The red and blue dashed lines indicate the average peak heat flux and sample thickness, respectively.

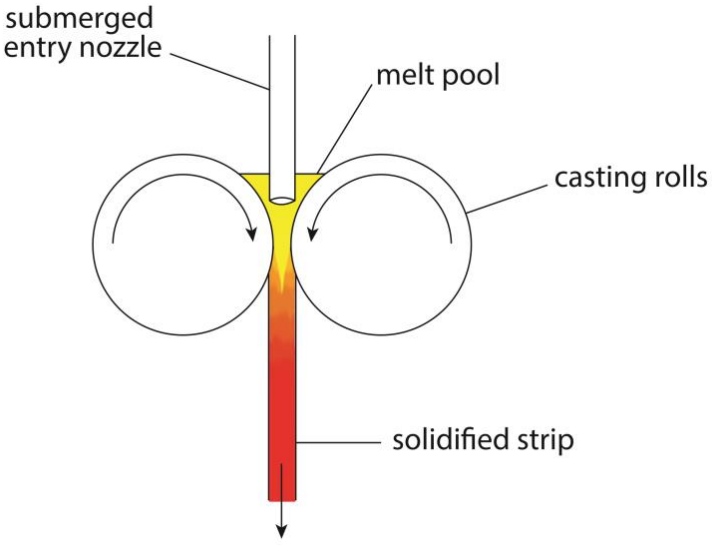

Figure 3.2. Schematic of the twin roll casting process.

For the work done here, the average heat flux was used instead of the peak heat flux to allow for comparisons to the amount of heat removed throughout the duration the strip moves through the casting rolls. The method of calculating the average heat flux, as shown in Equations 2-1 and 2-2, was less prone to inaccuracies due to the transient conditions as well.

3.1.2. Comparison to Other Work. A review of literature containing other dip testing systems showed typical peak heat fluxes of 8-12 MW/m^2 in various alloy systems [89]. Strezov et al. showed that after several successive of dips, the peak heat flux could be increased by more than 4 times the initial values [89]. The initial heat fluxes of 9-11 MW/m^2 increased to 43-47 MW/m^2 in the 304 stainless steel they tested. This increase in heat flux was the result of a buildup of manganese-silicates on the Cr-coated surface of the blocks. Once the blocks were sufficiently coated, the oxide melted and re-solidified on the surface causing reheating of the interfacial shell and leading to the increased heat transferred. The remelting of the manganese-silicates resulted in an increase in the size of the oxide particles from 5-8 μm to 25 μm. The remelting also served to keep the oxide layer at an optimum thickness where the larger heat fluxes were sustained through successive dips.

Although the copper blocks were cleaned with a brass wire brush after each dip in the work here, MnO was observed to form on the surface of the blocks after the 6 dips during testing of Alloy 7, as shown in Figures 3.3 a-h. This oxide caused a modest increase in the peak heat flux through resistive heating and reheating of the shell as more MnO solidified on the surface of the blocks, as shown for the increases in manganese content during the dip testing of Alloy 1 in Figure 3.4. The size of the oxide particles found on the surface of the blocks shown in Figure 3.5 did not increase, which is evidence that the oxide did not fully remelt and grow.

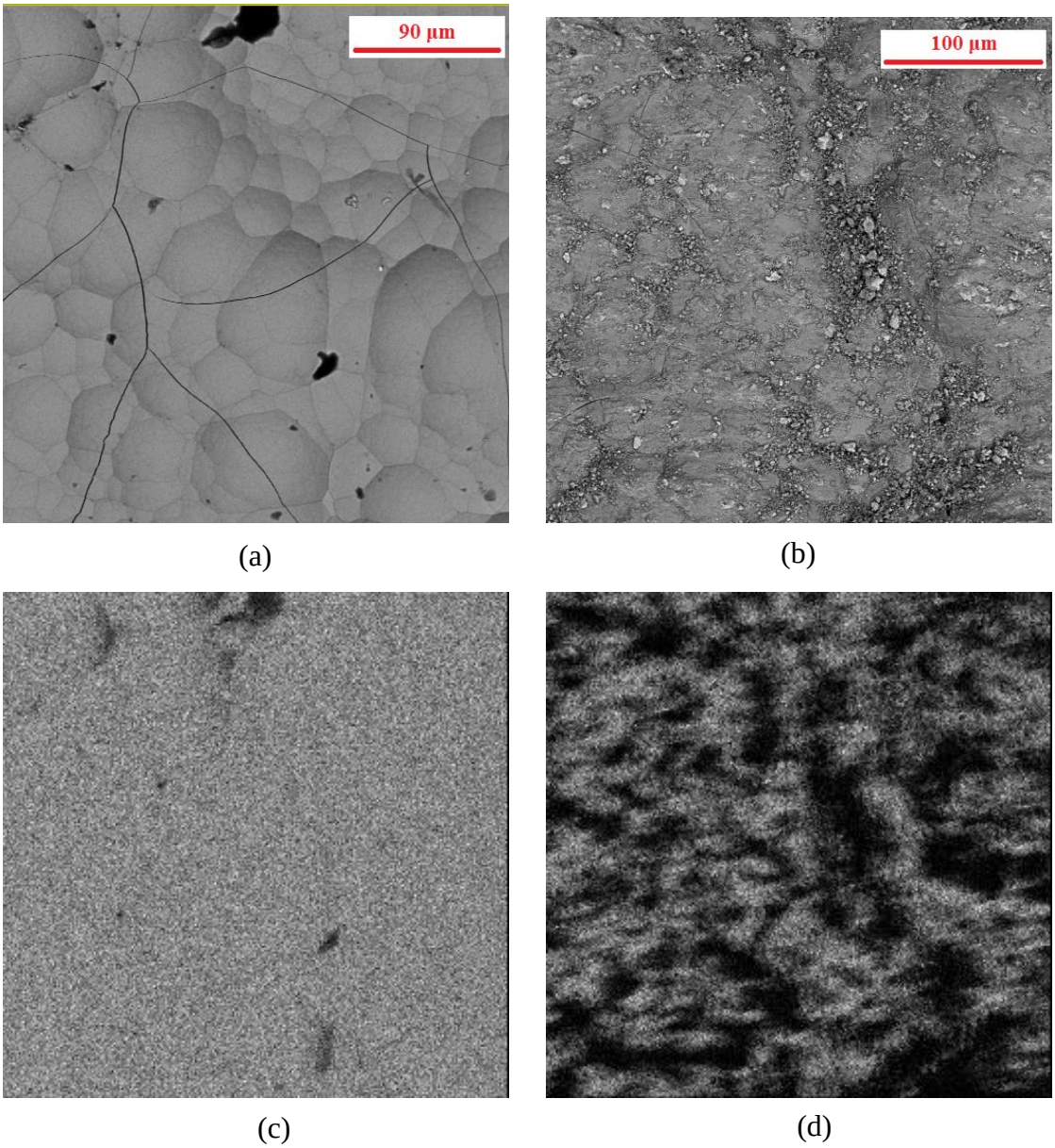

Figure 3.3. Backscattered electron images (BEI) and compositional maps of a new Cr-coated copper block and the used Cr-coated copper block after 6 dips of testing Alloy 7. (a) BEI of the new Cr-coated copper block and (b) BEI of the used Cr-coated copper block. Elemental maps of (c) Cr on the new block, (e) Mn on the new block, (g) oxygen on the new block, (d) Cr on the used block, (f) Mn on the used block, and (h) oxygen on the used block. All elemental maps were taken at the same magnification as the BEI image.

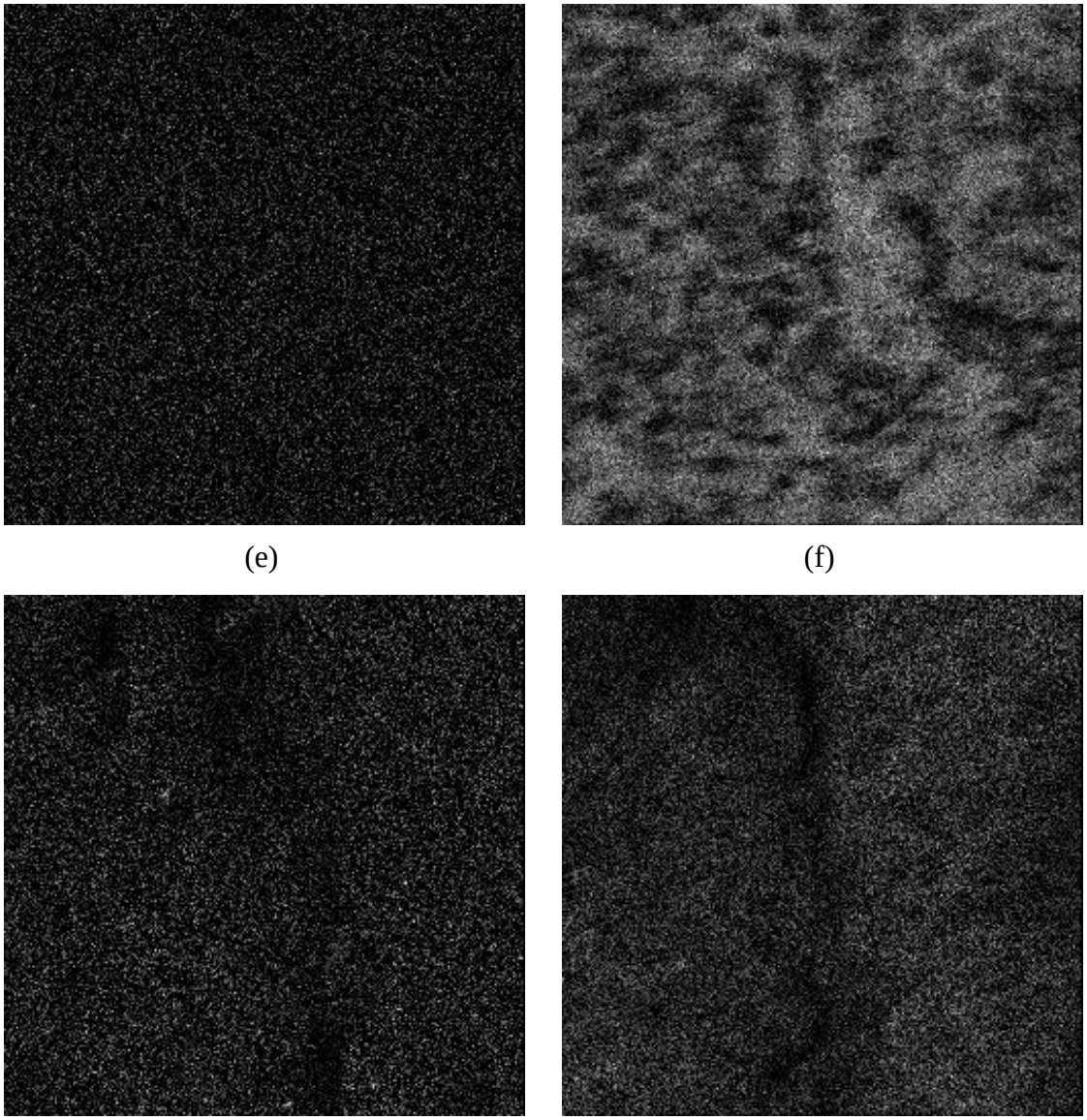

(e) (f)

(g) (h)

Figure 3.3. Backscattered electron images (BEI) and compositional maps of a new Cr-coated copper block and the used Cr-coated copper block after 6 dips of testing Alloy 7. (a) BEI of the new Cr-coated copper block and (b) BEI of the used Cr-coated copper block. Elemental maps of (c) Cr on the new block, (e) Mn on the new block, (g) oxygen on the new block, (d) Cr on the used block, (f) Mn on the used block, and (h) oxygen on the used block. All elemental maps were taken at the same magnification as the BEI image (cont.)

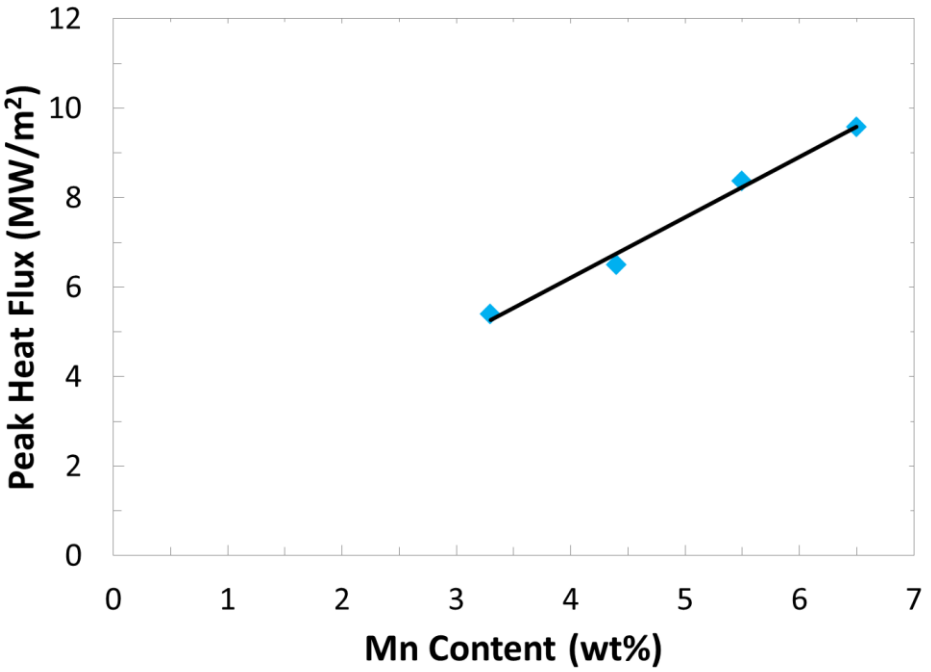

Figure 3.4. Mn content vs. peak heat flux for Alloy 1 (0.3 wt% C and 0.3 wt% Si).

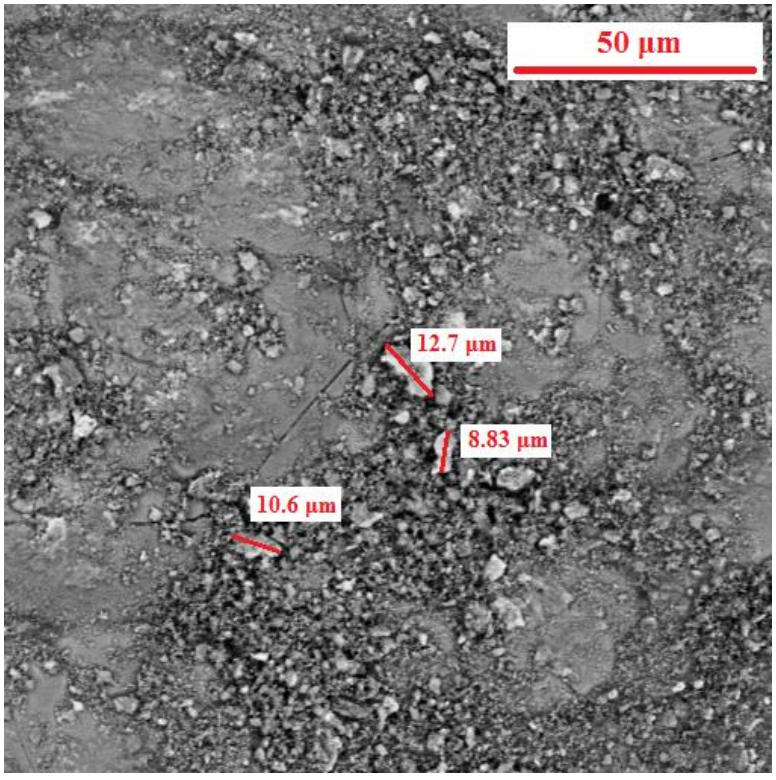

Figure 3.5. Size of the MnO particles on the block after the 6 dips during Alloy 7.

Another difference between the work done here and previous work is that the copper blocks were allowed to cool to between 30-70°C before the next dipping sequence was performed. In literature, the blocks were kept as hot as 120°C [89]. In the experiments performed here, the blocks were allowed to cool for a consistent starting point prior to each dip. A 14% increase in the heat flux was noticed even in the moderate difference from 30°C to 70°C in this work.

3.2. THERMOFLUID MODELING

Air pockets present in many samples, as shown in Figure 3.6, suggested the existence of air gaps between the solidifying sample and the copper blocks. The interfacial gas/air gap has been documented for dip testing [56,59,89] and for horizontal single belt casting simulation [72,91]. Thermofluid modeling with ANSYS Fluent was used to examine the effect of this air gap on the sample thickness and average heat flux.

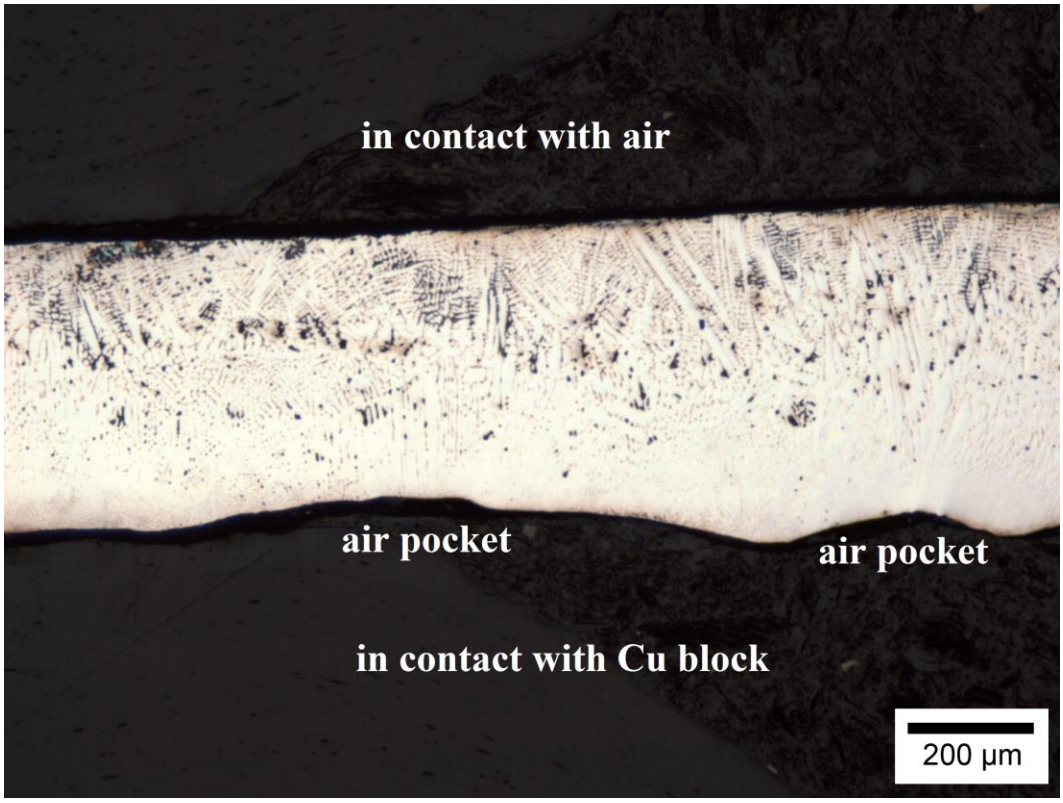

Figure 3.6. Air pockets caused by an air gap between the solidifying sample and the copper block.

For the 0.2 seconds the copper blocks spent in the melt, the calculated heat flux and sample thickness expectedly decreased with an increase in the thickness of the air gap. This is plotted in Figure 3.7.

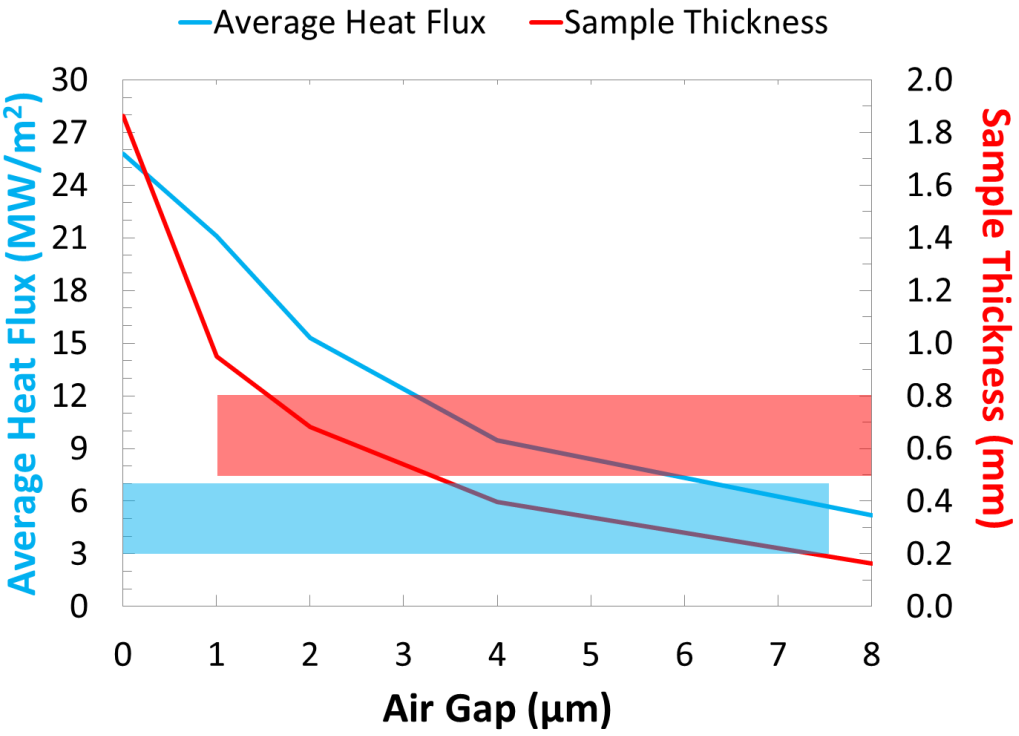

Figure 3.7. The average heat flux and shell thickness of samples dip tested with various air gaps from ANSYS Fluent simulations. The blue and red bars indicate the ranges of average heat fluxes and sample thicknesses measured experimentally in this work.

The simulation is far more ideal than the experiment, resulting in different average heat fluxes than were seen experimentally. The sample thickness, however, gives a good approximation for the encountered air gap during dip testing and is not subject to variations in the measurement system. Pairing the experimental data with the simulations, the experimental sample thicknesses suggest an air gap of 1-3 µm is reasonable.

3.3. EFFECT OF ALLOYING ELEMENTS ON HEAT TRANSFER

The primary alloying elements, superheat during dipping, and dipping speed had detectable effects on the heat transfer, and the subsequent sample thickness. An explanation for each of the effects is given here, using thermodynamics, kinetics, and material properties.

3.3.1. Effect of Manganese. Manganese, the key alloying element in the 3rd generation alloys studied here improved the heat flux and k-factor for both low and high manganese alloys. The trend of increasing heat flux at low manganese contents (3-7 wt%) was shown in Figure 3.4 for Alloy 1. The k-factor, which is directly related to the heat flux as shown in Figure 1.6, increased for the high manganese contents of Alloy 7 (10-20 wt%) and is shown in Figure 3.8.

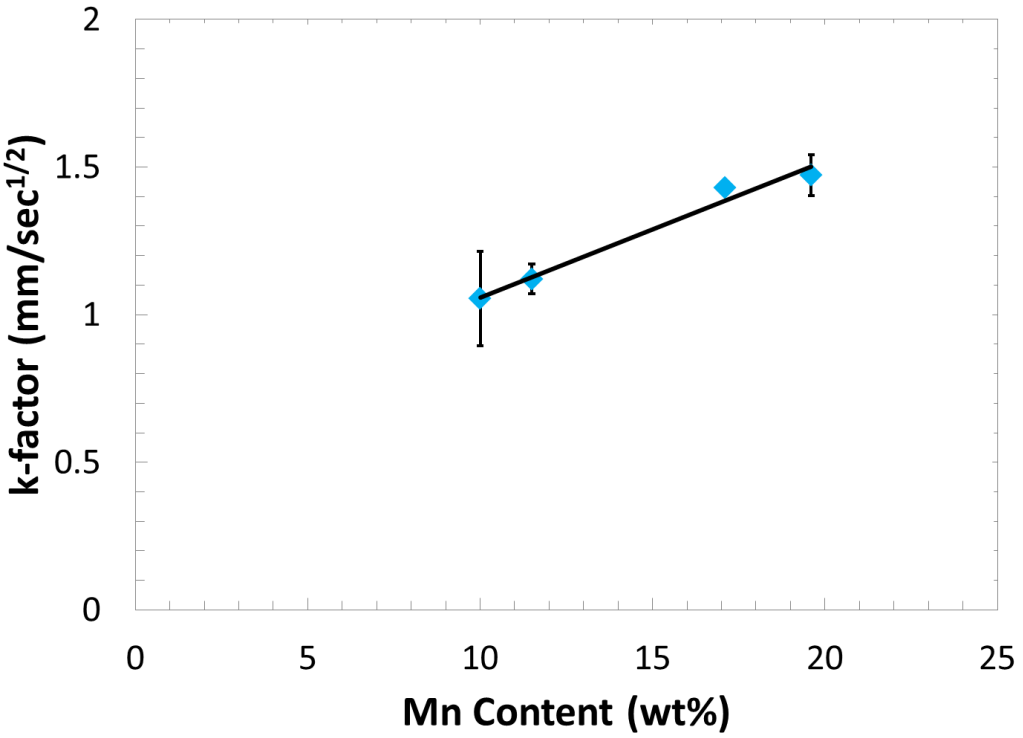

Figure 3.8. Mn content vs. k-factor for Alloy 7 (0.18 wt% C, 2.7 wt% Si, and 0.1 wt% Al). The error bars represent a 95% confidence level in the measurement of the thickness of the samples.

As was explained in Section 3.1.2, dipping in Mn-containing alloys coats the copper blocks with MnO and increases the heat flux through both solidification and conduction. The MnO layer reduces the air gap, improving the contact between the blocks and the sample. This was seen by a reduction in the amount and depth of the air pockets in Figures 3.9 a, b, and c. Another cause for the decrease in the air pockets in the samples of Figure 3.9 is that the increasing amounts of manganese move the solidification path to primary austenite rather than the peritectic transformation in some of the alloys tested. The peritectic transformation causes a volume contraction. In dip testing, the peritectic transformation causes the sample to pull away from the surface on which it solidifies since it is not constrained at the side opposite the copper block. In industry, this is the cause of many continuous casting issues, and the region of peritectic transformation is typically avoided to reduce the metallurgical length- which was described in Section 1.1.3.1- and successfully produce steel strip.

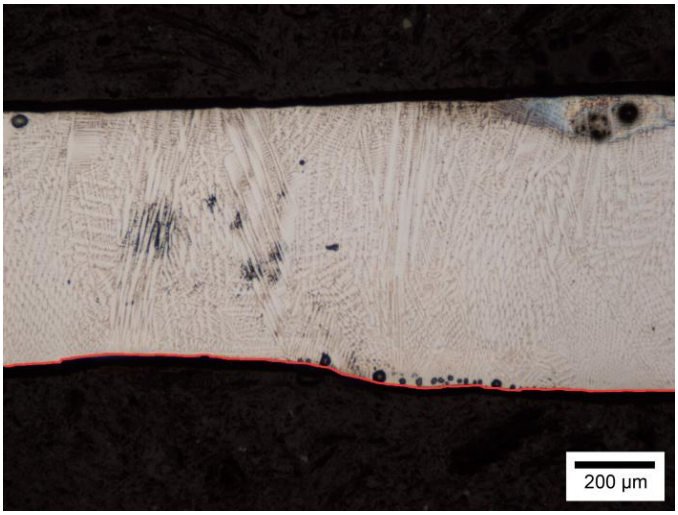

(a)

Figure 3.9. Air pockets in the Alloy 5.2 samples after consecutive dips. (a) 1 dip, (b) 2 dips, and (c) 5 dips. The surface in contact with the copper block is at the bottom of each image. The red line highlights the sample boundary.

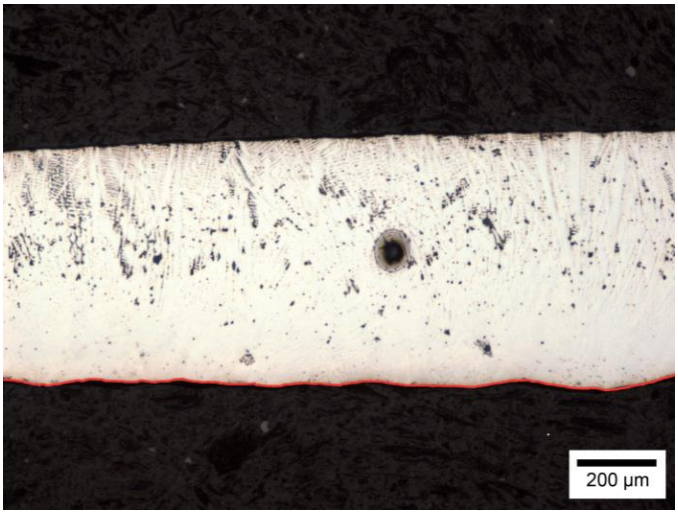

(b)

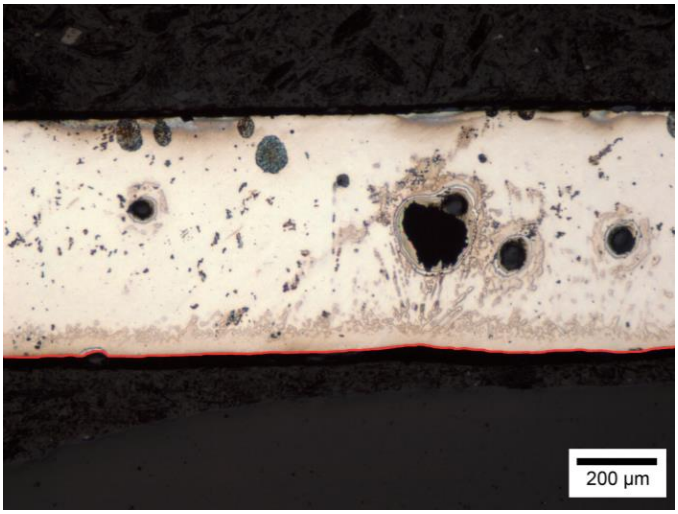

(c)

Figure 3.9. Air pockets in the Alloy 5.2 samples after consecutive dips. (a) 1 dip, (b) 2 dips, and (c) 5 dips. The surface in contact with the copper block is at the bottom of each image. The red line highlights the sample boundary (cont.).

The reason more MnO forms on the blocks more so than other oxides can be demonstrated by FactSage calculations, as shown in Figure 3.10. Figure 3.10 demonstrates that MnO forms more favorably than SiO_2 when the manganese content was greater than 7 wt% and the silicon content was less than 2.5 wt%. The high activity

of manganese at high manganese contents and low oxygen activity from dipping under inert gas atmospheres do not allow for the formation of silicates on the copper blocks.

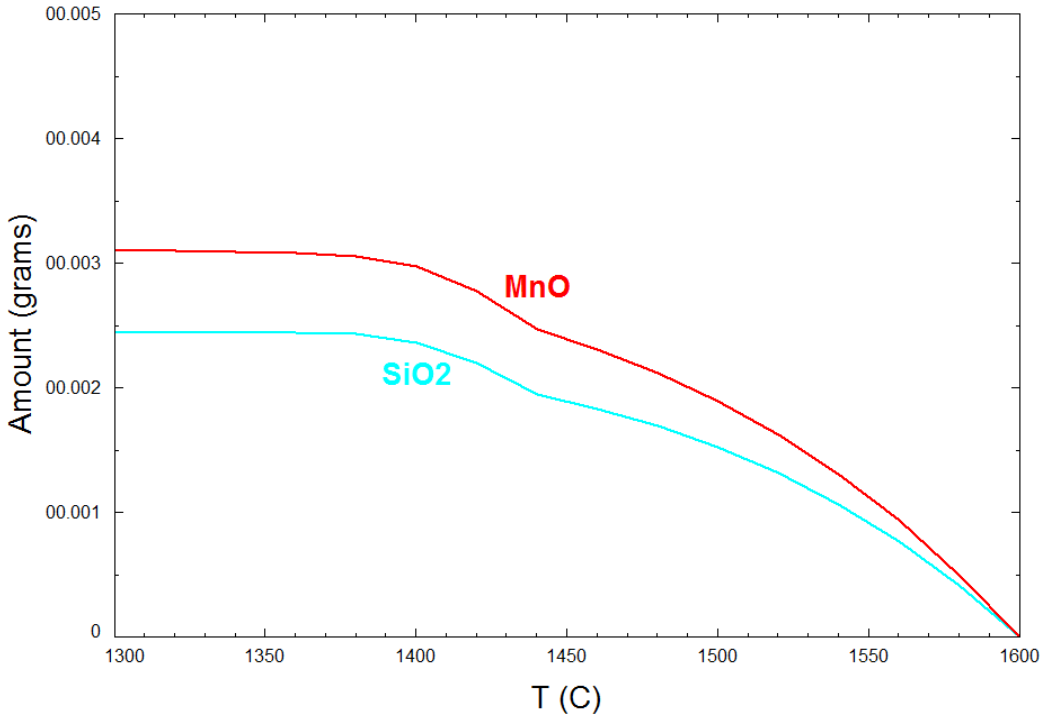

Figure 3.10. FactSage calculations of the stable oxide formation in an alloy of 0.3 wt% C, 2.5 wt% Si, 7 wt% Mn, and 50 ppm O.

The high aluminum contents in some of the alloys studied produces an aluminum oxide that is more stable than the manganese oxide. However, these solid alumina inclusions float out of the melt and are easily removed when the melt is de-slagged. Manganese remains in solution and is free to form an oxide once exposed in the air gap during dipping. The MnO can also remain a viscous liquid by forming a lower melting point slag with FeO than Al_2O_3 does.

3.3.2. Effect of Aluminum. Aluminum was observed to increase the heat flux. Additions of aluminum in Alloy C increased the average heat flux as shown in Figure 3.11.

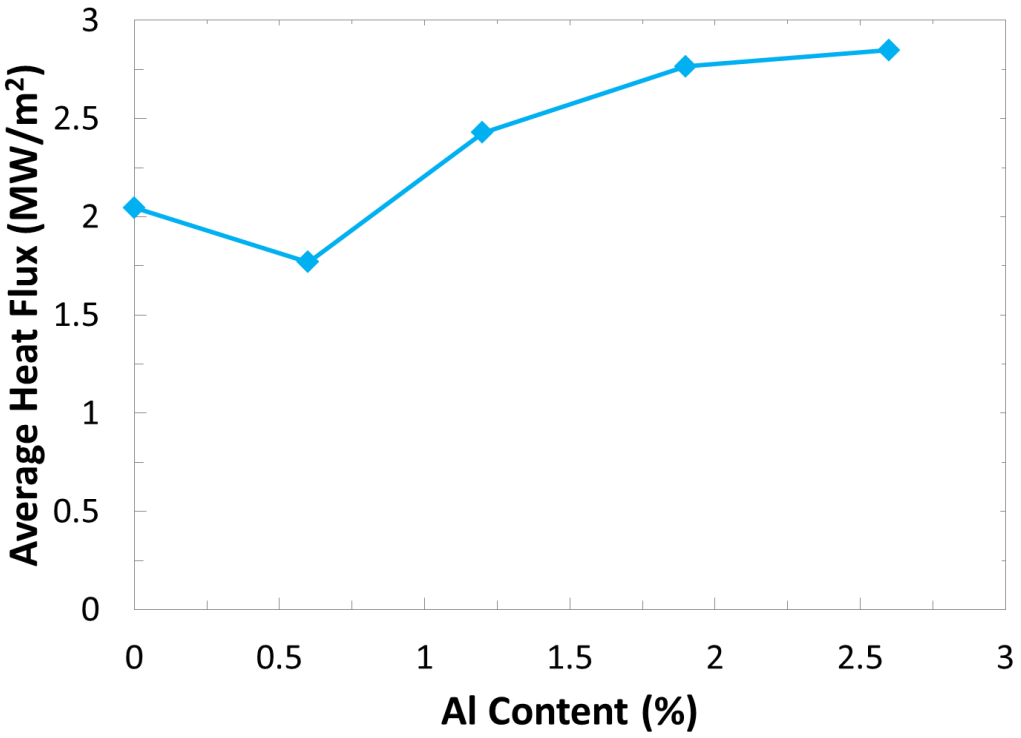

Figure 3.11. Aluminum content vs. average heat flux for Alloy C (0.25 wt% C, 0.6 wt% Mn, and 2.5 wt% Si).

Aluminum additions cause solidification of the melt into two- and three-phase regions as shown in Figure 3.12. The effect of aluminum on the solidification path is illustrated in Figure 3.13 where the enthalpy released during solidification is larger with increasing aluminum contents. The difference in the enthalpy of the liquid at the initial dipping temperature and the solidus point for each alloy indicates the amount of heat that is released during solidification.

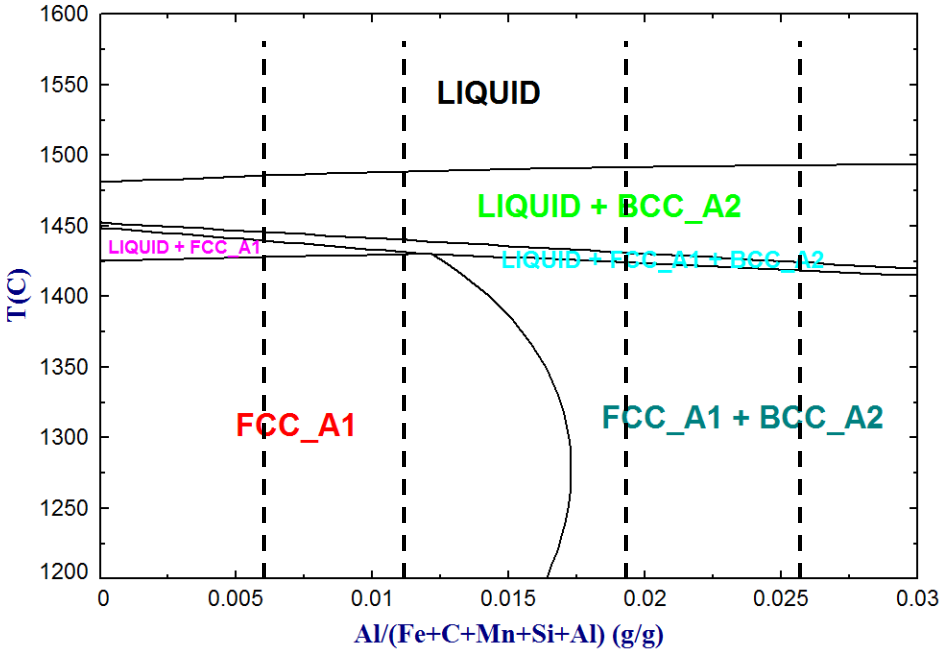

Figure 3.12. Phase diagram for Alloy C with varying aluminum contents, as calculated with FactSage. The dashed lines indicate the aluminum contents of Alloy C.

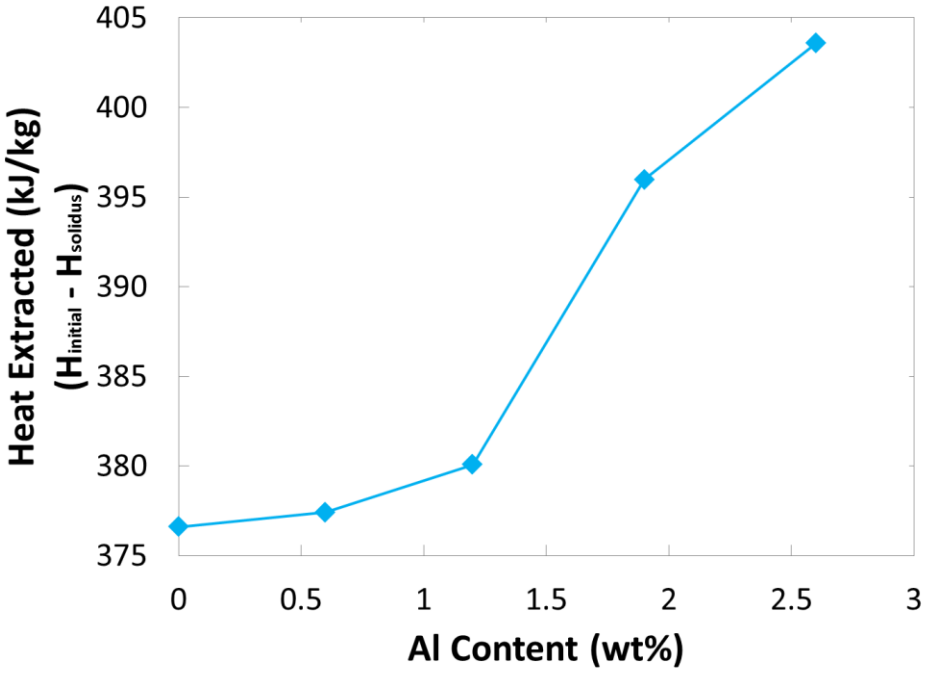

Figure 3.13. The amount of heat released during solidification from the initial dipping temperature to the solidus temperature for varying aluminum contents of Alloy C, as calculated with FactSage. The average superheats for the two dips of each composition provided in Table 2-2 were used as the initial temperature.

Another effect of aluminum is the reduction of MnO off the blocks upon reentering the melt. Aluminum is capable of reducing MnO to form Al_2O_3 and manganese in solution within the steel melt. At lower manganese contents, a stable oxide layer forms on the blocks through a balance of the formation of the MnO layer and reduction of this layer by aluminum. When the manganese content is increased above about 10 wt%, the aluminum additions are not as effective and the heat flux remains constant.

In this case, an increase in the heat flux was not without its penalties. Aluminum also has the effect of increasing the freezing range as can be seen in Figure 3.12. This was found to have the negative effect of increasing the SDAS in Alloys C-6, C-8, and C-10. This is shown in Figure 3.14. Larger SDAS increases the propensity for segregation and banding. As was described by Gigacher et al. in Section 1.1.1, the dendritic and banded microstructure requires extensive heat treatments to remove [8].

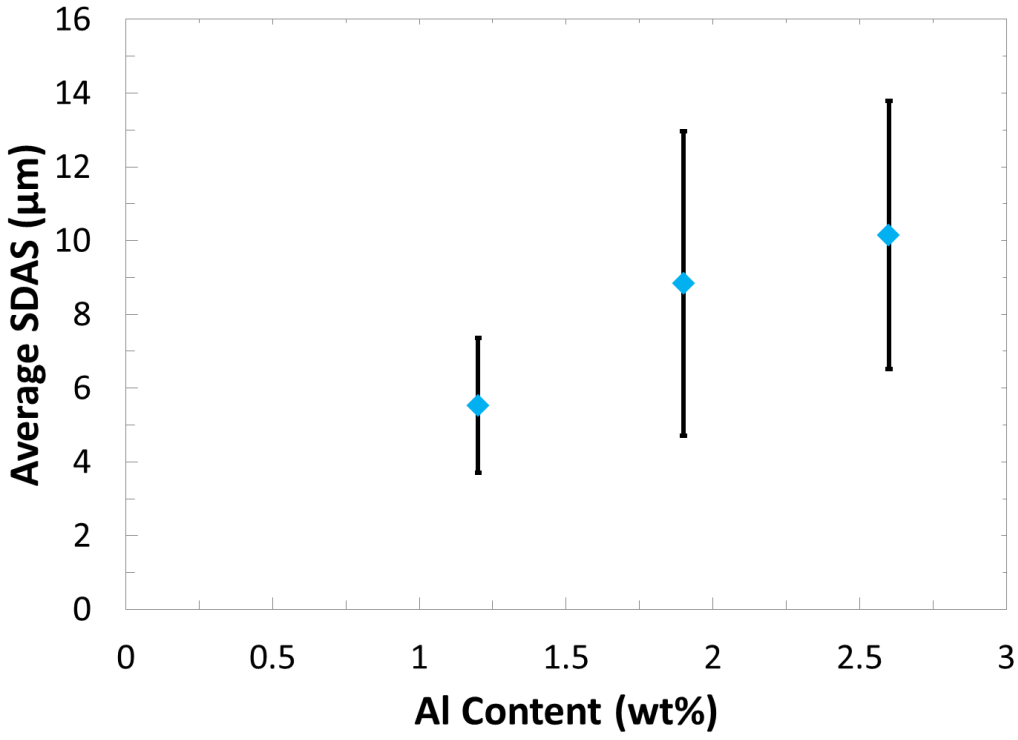

Figure 3.14. Aluminum content vs. average secondary dendrite arm spacing (SDAS). Error bars indicate a 95% confidence level of the measurements.

3.3.3. Effect of Silicon. Additions of silicon were seen to have no effect on the heat flux. The silicon content was varied while keeping the manganese and carbon levels constant in Alloys 2A and 2C. As shown in Figure 3.15, the average heat flux does not change with increasing silicon content. Again, the alloy with higher manganese- in this case Alloy 2C- has the higher average heat flux under the same casting conditions.

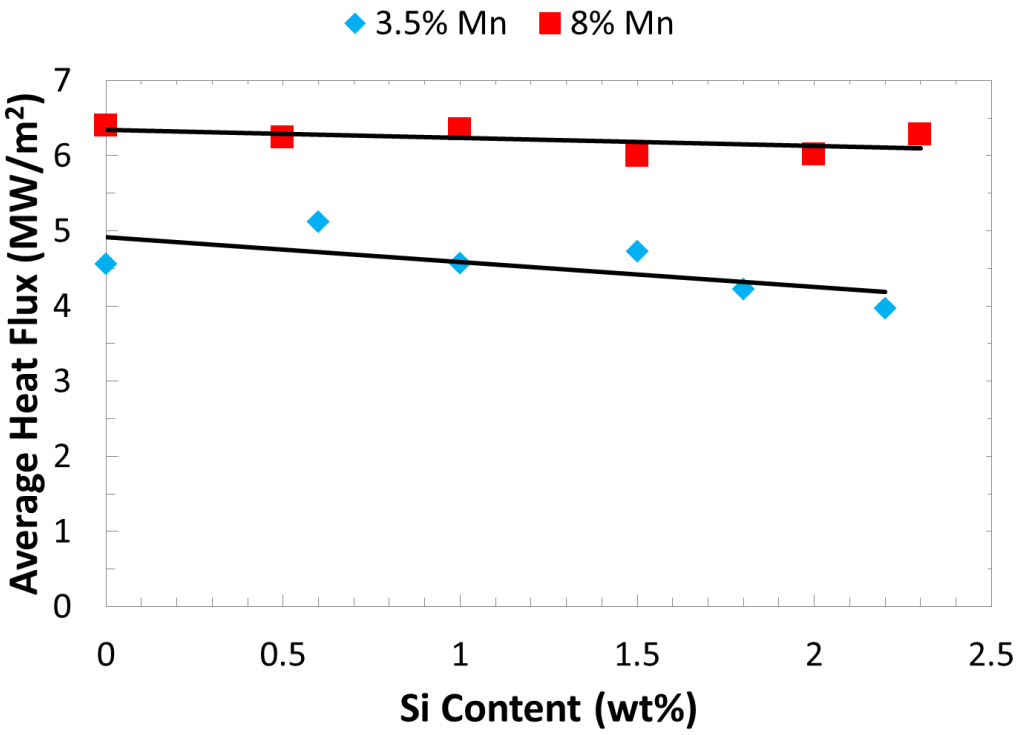

Figure 3.15. Silicon content vs. average heat flux for Alloys 2A (0.2 wt%C and 3.5 wt% Mn) and 2C (0.2 wt% and 8 wt%).

In an analysis of the changes silicon produces on the solidification path, it was observed that silicon additions in the range studied here had little or no effect on changing the freezing range or the phases formed on solidification. As was mentioned in Section 3.1.2, silicon is not present in the oxide that forms on the copper blocks and therefore does not improve or detract from the heat transfer.

3.3.4. Effect of Carbon. The effect of carbon on the solidification characteristics of these alloys was not well-characterized because the contents were within a narrow range, between 0.2-0.3 wt%. They were also never varied more than once within one test heat.

3.3.5. Effect of Superheat and Dipping Speed. Increases in both the superheat and the casting speed were seen to increase the average heat flux when Alloy AC was tested. During the test, the composition was kept the same while the superheats and dipping speeds were varied. The resulting data is presented in Figure 3.16.

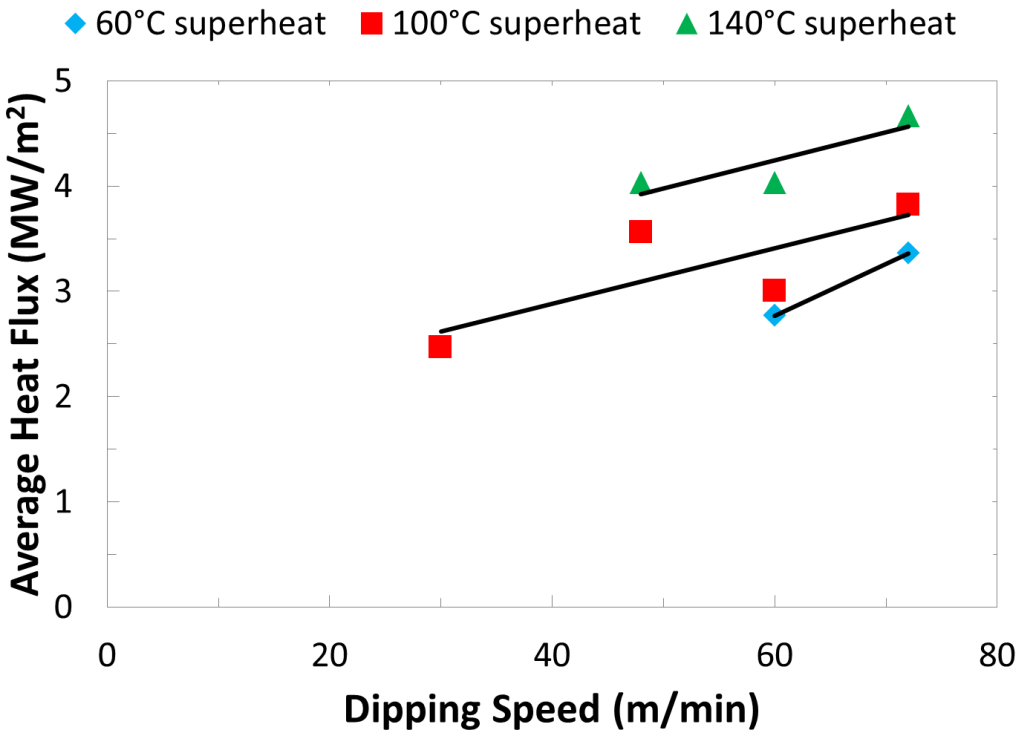

Figure 3.16. Average heat flux as a function of casting speed and superheat for Alloy AC (0.2 wt% C, 7.5 wt% Mn, 2.5 wt% Si, and 2 wt% Cu).

Increasing the superheat raised the heat flux by making the melt less viscous, therefore increasing the wettability between the melt and the copper blocks. The increase in wettability provided better contact with the copper blocks [56]. The increased temperature also produced a larger temperature difference between the solidifying sample

and the copper blocks, increasing the rate of heat flow. This was observed previously [56].

An increase in the dipping speed was also observed to increase the average heat flux in this alloy. Although an increase in dipping speed up to 72 meters per minute increased the average heat flux here, it is anticipated that there exists an optimum dipping speed; above which the heat flux decreases. This is a result of the solidification time, or dipping time, approaching the time to reach the peak heat flux. The average heat flux is reduced as the length of time spent at the peak heat flux is reduced. The optimum casting speed is different for each alloy and is dependent upon variables such as the k-factor and superheat, as described in Section 1.1.3.1.

4. CONCLUSIONS AND RECOMMENDATIONS FOR FUTURE WORK

4.1. CONCLUSIONS

A literature survey was conducted prior to beginning research to determine the most efficient lab-scale method of testing the processing variables present in rapid solidification processing. From this search, dip testing was determined to be the best option. A dip tester was designed and built at Missouri University of Science and Technology to test promising 3rd generation AHSS alloys. From the work done on the several alloys contained here, conclusions were drawn about the effects of alloying elements of Mn, Si, and Al, dipping superheat, and dipping speed.

The compositional variables which increased the heat flux and k-factor in this work were additions of manganese and aluminum. The process variables which increased the heat flux were higher superheats and faster casting speeds. The alloying additions, however, had a detrimental effect of increasing the solute segregation within the dip test samples. The addition of silicon appeared to have no effect on changing the heat flux.

Several mechanisms govern the occurrence of the above-mentioned trends. MnO formation on the copper blocks increases the heat transfer by reducing the air gap between the solidifying sample and the copper blocks and increasing the conductive heat transfer. Phase transformations increase the amount of heat (enthalpy) released during solidification and increase the heat flux, however at the cost of segregation in the microstructures. Large freezing ranges increase the secondary dendrite arm spacings allowing for more segregation and making homogenization more difficult. An increase in the superheat increased the heat flux by decreasing the melt viscosity and improving the wetting between the melt and copper blocks. An increase in the dipping speed increased the heat flux as well. However, there is likely an optimum dipping speed above the range studied at which the heat flux is a maximum.

4.2. RECOMMENDATIONS FOR FUTURE WORK

Pertaining to the dip tester, the maneuverable lift that holds the dip tester should be made more rigid to ensure the dip is not subject to disturbances as it enters and exits the melt. The process of recording and analyzing the temperature data could be improved

through the programming of a trigger and instantaneous conversion to temperature and heat flux within the temperature recording system. This could be done through LabView and example files are on-hand. Additional future work for the dip tester is provided in the Appendix.

Tests should be run where the oxide layer is allowed to build up during a dip test to verify the heat flux can be drastically increased through this phenomenon. Dip testing one of the alloys produced at Castrip daily would provide a beneficial benchmark for dip testing other developmental alloys.

APPENDIX

DIP TESTER USER GUIDE

The user guide for the dip tester has been removed at the request of the industry sponsor.

BIBLIOGRAPHY

[1] R. Pla-Ferrando, S. Sanchez, M. A. Selles, and A. V. Martinez-Sanz "TWIP/TRIP Steels. Future Trends in Automotive Industries," *Annals of the Oradea University*, Fascile of Management and Technological Engineering, Volume X (XX), 2011, NR3

[2] R. Kuziak, R. Kawalla, and S. Waengler "Advanced High Strength Steels for Automotive Industry," *Archives of Civil and Mechanical Engineering*, Vol. 8 No. 2, 2008, pp. 103-117

[3] O. Grassel, L. Krüger, G. Frommeyer, and L. W. Meyer "High Strength Fe-Mn-(Al, Si) TRIP/TWIP Steels Dveleopment – Properties – Application," *International Journal of Plasticity*, Vol. 16, 2000, pp. 1391-1409

[4] S. T. Pisarik, D. C. Van Aken, K. R. Limmer, and J. E. Medvedeva "Developing a Third-Generation Advanced High-Strength Steel with Two-Stage TRIP Behavior," *AISTech 2014 Conference Proceedings*, Indianapolis, Indiana, 2014, pp. 3013-3023

[5] David K. Matlock and John G. Speer "Processing Opportunities for New Advanced High-Strength Sheet Steels," *Materials and Manufacturing Processes*, Vol. 25, 2010, pp. 7-13

[6] B. C. De Cooman, O. Kwon, and K. G. Chin "State-of-the-Knowledge on TWIP Steel," *Materials Science and Technology*, Vol. 28 No. 5, pp. 513-527

[7] Y. N. Datsur, W. C. Leslie, *Metallurgical and Materials Transactions A*, Vol. 12A, 1981, p. 749

[8] G. Gigacher, R. Pierer, J. Wiener, and C. Bernhard "Metallurgical Aspects of Casting High-Manganese Steel Grades," *Advanced Engineering Materials*, Vol. 8 No. 11, 2006, pp. 1096-1100

[9] H. Mizukami, A. Yamanaka, and T. Watanabe, *ISIJ International*, Vol. 42, 2002, p. 964

[10] M. Daamen, B. Wietbrock, S. Richter, and G. Hirt "Strip Casting of a High-Manganese Steel (FeMn22C0.6) Compared with a Process Chain Consisting of Ingot Casting and Hot Forming," *Steel Research International*, Vol. 82 No.1, 2011, pp. 70-75

[11] S. H. Wang, Z. Y. Liu, W. N. Zhang, G. D. Wang, J. L. Liu, and G. F. Liang "Microstructure and Mechanical Property of Strip in Fe-23Mn-3Si-3Al TWIP Steel by Twin Roll Casting," *ISIJ International*, Vol. 49 No. 9, 2009, pp. 1340-1346

[12] H. Chen, S. B. Kang, H. Yu, H. W. Kim, and G. Min, *Materials Science and Engineering A*, Vol. 492, 2008, p. 317

[13] Teresa Lis "Modification of Oxygen and Sulfur Inclusions in Steel by Calcium Treatment," *Metalurgija*, Vol. 48 No.2, 2009, pp. 95-98 (translated to English)

[14] Total Materia, "Clean Steel: Part Three" 2007

[15] A. Grajcar, U. Galisz, and L. Bulkowski "Non-Metallic Inclusions in High Manganese Austenitic Alloys," *Archives of Materials Science and Engineering*, Vol. 50 No. 1, 2011, pp. 21-30

[16] A. Grajcar "Modification of Non-Metallic Inclusions by Rare-Earth Elements in Low-Alloyed C-Mn-Si-Al-type Steels," *Ores and Metals*, Vol. 55 No. 3, 2010, pp. 143-152 (in Polish)

[17] K. Bolanowski "Influence of Rate-Earch Elements on the Structure and Properties of Steel," *Metallurgical News*, Vols. 7-8, 2004, pp. 323-325 (in Polish)

[18] S. T. Pisarik and D. C. Van Aken, 2014 "Thermodynamic Driving Force of the $\gamma \rightarrow \varepsilon \rightarrow \alpha'$ Transformation in FeMnAlSiC Steels" currently unpublished (to be published in Met Trans A)

[19] M. Daamen, O. Guvenc, M. Bambach, and G. Hirt "Development of Efficient Production Routes Based on Strip Casting for Advanced High Strength Steels for Crash-Relevant Parts," *CIRP Annals - Manufacturing Technology*, 2014

[20] Markus Daamen, Silvia Richter, and Gerhard Hirt "Microstructure Analysis of High-Manganese TWIP Steels Produced via Strip Casting," *Key Engineering Materials*, Vols. 554-557, 2013, pp. 553-561

[21] A. Grajcar, R. Kuziak, and W. Zalecki "Third Generation of AHSS with Increased Fraction of Retained Austenite for the Automotive Industry," *Archives of Civil and Mechanical Engineering 12*, 2012, pp. 334-341

[22] W. C. Jeong, D. K. Matlock, and G. Krauss "Observation of Deformation and Transformation Behavior of Retained Austenite in a 0.14%C-1.2%Si,1.5%Mn Steel with Ferrite-Bainite-Austenite Structure," *Materials Science and Engineering*, Vol. A165,1993, pp. 1-8

[23] Huseyin Aydin, Elhachmi Essadiqi, In-Ho Jung, and Stephen Yue "Development of 3rd Generation AHSS with Medium Mn Content Alloying Compositions," *Materials Science and Engineering A*, Vol. 562, 2013, pp. 501-508

[24] Codrick J. Martis, Susil K. Putatunda, and James Boileau "Processing of a New High Strength High Toughness Steel with Duplex Microstructure (Ferrite + Austenite)," *Materials and Design*, Vol. 46, 2013, pp. 168-174

[25] P. Duwez "Metastable Phases Obtained by Rapid Quenching from the Liquid State," *Progress in Solid State Chemistry,* Vol. 3, 1967, pp. 377-406

[26] L. Jacobson and J. McKittrick "Rapid Solidification Processing," *Materials Science and Engineering: R,* Vol. 11, 1994, pp. 355-408

[27] W. Kurz and R. Trivedi "Rapid Solidification Processing and Microstructure Formation," *Materials Science and Engineering A,* Vols. 179/180, 1994, pp. 46-51

[28] C. P. Manning and R. J. Fruehan "Emerging Technologies for Iron and Steelmaking," *JOM,* Vol. 53 No. 10, 2001, pp. 20-23

[29] M. Ferry "Direct Strip Casting of Metals and Alloys," W*oodhead Publishing in Materials,* 2006, pp.1-255

[30] N. Li, Z. Y. Liu, Z. S. Lin, Y. Q. Qiu, X. H. Liu, and G. D. Wang "Solidification Structure of Strip Cast Low Carbon Steels with Phosphourus Addition," *Journal of Materials Science and Technology*, 2006, Vol. 22, pp. 1-5

[31] K. H. Spitzer, F. Ruppel, R. Viscorova, R. Scholz, J. Kroos, and V. Flaxa "Direct Strip Casting (DSC)—An Option for the Production of New Steel Grades," *Steel Research,* Vol. 74, 2003, pp. 724-731

[32] Z. Y. Liu, Z. S. Lin, S. H. Wang, Y. Q. Qiu, X. H. Liu, and G. D. Wang "Microstructure Characterization of Austenitic Fe-25Mn-22Cr-2Si-0.7N Alloy Processed by Twin Roll Strip Casting," *Materials Characterization*, Vol. 58, 2007, pp. 974-979

[33] R. Ueji, N. Tsuchida, D. Terada, N. Tsuji, Y. Tanaka, A. Takemura, and K. Kunishige "Tensile Properties and Twinning Behavior of High Manganese Austenitic Steel with Fine Grained Structure," *Scripta Materialia,* Vol. 59, 2008, pp. 963-966

[34] M. R. Barnett "A Rationale for the Strong Dependence of Mechanical Twinning on Grain Size," *Scripta Materialia*., Vol. 59, 2008, pp. 696-698

[35] K. Ishida and T. Nishizawa "Effect of Alloying Elements on Stability of Epsilon Iron," *Transactions of the Japan Institute of Metals,* Vol. 15, 1974, p. 225

[36] J.-E. Jin and Y.-K. Lee "Effects of Al on Microstructure and Tensile Properties of C-bearing High Mn TWIP Steel," *Acta Materialia,* Vol. 60, 2012, pp. 1680-1688

[37] D. C. Van Aken, Scott Pisarik, and M. C. McGrath "TRIP Behavior of Austenite and ε-Martensite Microstructures," *International Symposium on New Developments in Advanced High Strength Steels,* pp. 119-129

[38] R. E. Schramm and R. P. Reed "Stacking Fault Energies of Seven Commercial Austenitic Stainless Steels," *Metallurgical and Materials Transactions A,* Vol. 6A, 1975, p. 1345

[39] H.K.D.H. Bhadeshia and D. V. Edmonds "Bainite in Steels: New Composition Property Approach: Part I," *Materials Science*, 1983, Vol. 17, pp. 411-419

[40] Ohjoon Kwon, Kyooyoung Lee, Gyosung Kim, and Kwang-Geun Chin "New Trends in Advanced High Strength Steel Developments for Automotive Application," *Materials Science Forum*, Vols. 638-642, 2010, pp. 136-141

[41] S. B. Lee, Gwangyang, Korea, *private communication with D. K. Matlock and J. G. Speer*, 2008

[42] B. X. Huang, X. D. Wang, Y. H. Rong, L. Wang, and L. Jin "Mechanical Behavior and Martensitic Transformation of an Fe-Mn-Si-Al-Nb Alloy," *Materials Science and Engineering A*, Vols. 438-440, 2006, pp. 306-311

[43] S. Ge, M. Isac, and R. I. L. Guthrie "Progress of Strip Casting Technology for Steel; Historical Developments," *ISIJ International*, Vol. 52 No. 12, 2012, pp. 2109-2122

[44] R. I. L. Guthrie "Steel Strips – The Long and Winding Road," *Iron and Steel Technology*, Vol.3 No. 9, Nov. 2006, pp. 104-114

[45] S. Ge, M. Isac, and R. I. L. Guthrie "Progress in Strip Casting Technologies for Steel; Technical Developments," *ISIJ International*, Vol. 53 No.5, 2013, pp. 729-742

[46] T. Staubli and A. Di Miele: CFD Review – "CFD Aids Development of New Casting Process," November 2002

[47] M. Godat, B. Steiner, A. Scholes, and T. Staubli: *5th European Continuous Casting Conference,* ATS, St. Denis, France, 2005, 432

[48] N. Zapuskalov, "Comparison of Continuous Strip Casting with Conventional Technology," *ISIJ International*, Vol. 43 No. 8, 2003, pp. 1115-1127

[49] C. Kohl "SMS Demag in Castrip Deal," *American Metal Market*, September 2000, p. 3

[50] A. N. Smirnov and V. M. Safonov "Metallurgical Miniworks: Past, Present, and Future," *Steel in Translation*, Vol. 37 No. 1, 2007, pp. 47-52

[51] M. Godat, B. Steiner, A. Scholes, and T. Staubli "MAINSTRIP Twin Roll Casting Production Plant," *Lucerne University of Applied Sciences and Arts brochure* (accessed 5/9/14)

[52] SMS Group: SMS Group Newsletter "BCT Belt Casting Plant Pre-Assembled," Vol. 19 No. 1, March 2012, p. 51

[53] N. Nikolovski, R. Mahapatra, and L. Strezov "Casting Steel Strip," U*S Patent 7,604,039*, October 2009

[54] J. Watson, *private communication*, 4 August 2014

[55] J. W. Elmer, S. M. Allen, and T. W. Edgar "Microstructural Development during Solidification of Stainless Steel Alloys," *Metallurgical Transactions A*, Vol. 20A, Oct. 1989, pp. 2117-2131

[56] K. Mukunthan, P. D. Hodgson, P. Sellamuthu, L. Strezov, Y. Durandet, and N. Stanford "Castability and Microstructural Development of Iron-based Alloys under Conditions Pertinent to Strip Casting – Specialty Fe-Cr-Al Alloys," *ISIJ International*, Vol. 53 No. 10, 2013, pp. 1803-1811

[57] K. Mukunthan, L. Strezov, R. Mahapatra, and W. Blejde "Evolution of Microstructures and Product Opportunities in Low Carbon Steel Strip Casting," *The Brimacombe Memorial Symposium*, Vancouver, Canada, Oct. 2000, pp. 1-16

[58] H. Zhao, D. Ju, and L. Hu "Evaluation on Microstructure of Thin Strip Produced by Twin-Roll Continuous Casting," *Journal of Material Science Technology*, Vol. 20, 2004, pp.105-107

[59] L. Strezov and J. Herbertson "Experimental Studies of Interfacial Heat Transfer and Initial Solidification Pertinent to Strip Casting," *ISIJ International*, Vol. 38 No. 9, 1998, pp.959-966

[60] J. V. Beck, B. Blackwell, and C. R. St. Clair "Inverse Heat Conduction: Ill-Posed Problems," John Wiley and Sons, New York, 1985

[61] T. Evans and L. Strezov "Interfacial Heat Transfer and Nucleation of Steel on Metallic Substrates," *Metallurgical and Materials Transactions B*, Vol. 31B, Oct. 2000, pp. 1081-1089

[62] J. V. Wood and R. W. K. Honeycombe "Splat Quenching of a Nickel-Chromium Steel containing Boron and Titanium Additions," *Materials Science and Engineering*, Vol. 38, 1979, pp. 217-226

[63] R. Mahapatra, W. Blejde, H. Fukase, P. Woodberry, M. Schlichting, and N. Ross "Commercial Production of Thin-Strip by Twin-Roll Strip Casting- CASTRIP Process," *TMS 2013 Annual Meeting Supplemental Proceedings*, 2013, pp. 431-438

[64] G. E. Lucas, G. R. Odette, and J. W. Sheckherd "Shear Punch and Microhardness Tests for Strength and Ductility Measurements," *The Use of Small-Scale Specimens for Testing Irradiated Material*, ASTM STP 888, W. R. Corwin and G. E. Lucas, Eds., American Society for Testing and Materials, Philadelphia, 1986, pp.112-140

[65] S. R. Chen, H. A. Davies, and W. M. Rainforth "Austenite Phase Formation in Rapidly Solidified Fe-Cr-Mn-C Steels," *Acta Materialia*, Vol. 47 No. 18, 1999, pp. 4555-4569

[66] R. B. Pond "Metallic Filaments and Method of Making Same," *US Patent 2,825,108*, March 1958

[67] M. Hanao, M. Kawamoto, and A. Yamanaka "Growth of Solidified Shell Just Below the Meniscus in Continuous Casting Mold," *ISIJ International*, Vol. 49 No. 3, 2009, pp. 365-374

[68] N. H. Pryds and A. S. Pedersen "Rapid Solidification of Martensitic Stainless Steel Atomized Droplets," *Metallurgical and Materials Transactions A*, Vol. 33A, Dec. 2002, pp. 3755-3761

[69] Y. J. Choi "Non-Equilibrium Solidification of Delta-TRIP Steel," *Master's Thesis*, Pohang University of Science and Technology, 2011

[70] C. Hayzelden, J. J. Rayment, and B. Cantor "Rapid Solidification Microstructures in Austenitic Fe-Ni Alloys," *Acta Metallurgica*, Vol. 31 No. 3, 1983, pp. 379-386

[71] D. Li, M. Isac, and R. Guthrie "Improving Strip Surface Quality of AA6111 Alloy using Different Casting Atmospheres for the Horizontal Single Belt Strip Casting (HSBC) Process," *Light Metals 2012*, TMS (The Minerals, Metals & Materials Society), 2012, pp. 1101-1105

[72] R. I. L. Guthrie, M. Isac, and D. Li "Ab-initio Predictions of Interfacial Heat Flows during the High Speed Casting of Liquid Metals in Near Net Shape Casting Operations," *Steel Research International*, Vol. 81 No. 10, 2010, pp. 891-898

[73] S. T. Lakshmikumar, R. M. Mallya, and E. S. R. Gopal "Development of a Roller Apparatus for the Production of Amorphous Phases," *Bulletin of Material Science*, Vol. 2 No. 4, Nov. 1980, pp. 233-237

[74] H.-U. Lindenberg, U. Albrecht-Fruh, M. Walter, R. Capotosti, G. Stebner, and D. Senk: *Forum- Technische Mitteilungen Thyssen Krupp* (English Edition), Dec. 2000, p. 20

[75] T. Matsushita, K. Nakayama, F. Hisahiko, and S. Osada "Development and Commercialization of Twin Roll Strip Caster," *IHI Engineering Review*, Vol. 42 No. 1, February 2009, pp. 1-9

[76] N. H. Pryds, T. W. Juhl, and A. S. Pedersen "The Solidification Characteristics of Laser Surface-Remelted Fe-12Cr-nC Alloys," Metallu*rgical and Materials Transactions A*, Vol. 30A, July 1999, pp. 1817-1826

[77] P. Pietrokowsky "Novel Mechanical Device for Producing Rapidly Cooled Metals and Alloys of Uniform Thickness," *Review of Scientific Instruments*, Vol. 34, 1963, pp. 445-446

[78] P. Duwez and R. H. Willens "Rapid Quenching of Liquid Alloys," *Transactions of the Metallurgical Society of AIME*, Vol. 227, April 1963, pp. 362-365

[79] R. C. Ruhl "Cooling Rates in Splat Cooling," Materials Science and Engineering, Netherlands, 1966, pp.313-320

[80] V. Venkateswara Rao "A Modified Gun Technique for Melt Quenching Reactive Alloys," *Indian Journal of Engineering and Materials Sciences*, Vol. 13, Oct. 2006, pp. 451-454

[81] E. J. Hall "Metal-Disintegrating Apparatus," *US Patent 1,501,449*, July 1924

[82] S. P. Mates and G. S. Settles "A Study of Liquid Metal Atomization using Close-Coupled Nozzles, Part 1: Gas Dynamic Behavior," *Atomization and Sprays*, Vol. 15, 2005, pp. 1-22

[83] S. P. Mates and G. S. Settles "A Study of Liquid Metal Atomization using Close-Coupled Nozzles, Part 2: Atomization Behavior," *Atomization and Sprays*, Vol. 15, 2005, pp. 1-19

[84] P. Sellamuthu, N. Stanford, and P. D. Hodgson "Recrystallization Kinetic Behavior of Copper-Bearing Strip Cast Steel," *Steel Research International*, Vol. 84, No. 9999, 2013, pp. 1-8

[85] M. B. Toloczko, A. Katsunori, M. L. Hamilton, F. A. Gamer and R. J. Kurtz "The Effect of Test Machine Compliance on the Measured Shear Punch Yield Stress as Predicted Using Finite Element Analysis," *Materials Transactions*, JIM, Vol. 41 No. 10, 2000, pp. 1356-1359

[86] C. J. Egan "Fractional Solidification Process," *US Patent 2,579,421*, December 1951

[87] A. L. Lux and M. C. Flemings "Refining by Fractional Solidification," *Metallurgical Transactions B*, Vol. 10B, 1979, pp. 71-78

[88] W. R. Wilcox "Fractional Solidification Phenomena," *Separation Science*, Vol. 4 No. 2, 1969, pp. 95-109

[89] L. Strezov, J. Herbertson, and G. R. Belton "Mechanisms of Initial Melt/Substrate Heat Transfer Pertinent to Strip Casting," *Metallurgical and Materials Transactions B*, Vol. 31B, 2000, pp.1023-1030

[90] D. Edelman, *private communication*, 30 October 2013

[91] R. I. L. Guthrie and M. Isac "Horizontal Single Belt Casting of Aluminum and Steel," *Steel Research International*, Vol. 85, 2014, pp.1-12

VITA

Kramer Michael Pursell earned his B.S. in Mechanical Engineering with a minor in Metallurgy from Trine University in May of 2012. He has worked to earn his M.S. in Metallurgical Engineering at the Missouri University of Science and Technology from August 2012 through January 2015.